A fractal model of earthquake occurrence: Theory, simulations and comparisons with the aftershock data

Journal of Physics: Conference Series **319** (2011) 012004 doi:10.1088/1742-6596/319/1/012004

A fractal model of earthquake occurrence: Theory, simulations and comparisons with the aftershock data

Pathikrit Bhattacharya

Department of Earth Sciences, Indian Institute of Technology, Roorkee, Uttarakhand, *247 667*, India
Department of Earth Sciences, University of Western Ontario, London, Ontario, *N6A 5B7*, Canada. (At present)
Department of Geosciences, Princeton University, Guyot Hall, Princeton, NJ, *08544*, USA. (From September 2011)

E-mail: pathikri@princeton.edu

Bikas K. Chakrabarti

Theoretical Condensed Matter Physics Division and Centre for Applied Mathematics and Computational Science, Saha Institute of Nuclear Physics, Kolkata, West Bengal, *700064*, India.

E-mail: bikask.chakrabarti@saha.ac.in

Kamal

Department of Earth Sciences, Indian Institute of Technology, Roorkee, Uttarakhand, *247 667*, India

E-mail: kamalfes@iitr.ernet.in

Abstract. Our understanding of earthquakes is based on the theory of plate tectonics. Earthquake dynamics is the study of the interactions of plates (solid disjoint parts of the lithosphere) which produce seismic activity. Over the last about fifty years many models have come up which try to simulate seismic activity by mimicking plate plate interactions. The validity of a given model is subject to the compliance of the synthetic seismic activity it produces to the well known empirical laws which describe the statistical features of observed seismic activity. Here we present a review of one such, purely geometric, model of earthquake dynamics, namely The Two Fractal Overlap Model. The model tries to emulate the stick-slip dynamics of lithospheric plates with fractal surfaces by evaluating the time-evolution of overlap lengths of two identical Cantor sets sliding over each other. As we show later in the text, some statistical aspects of natural seismicity are naturally captured by this simple model. More importantly, however, this model also reveals a new statistical feature of aftershock sequences which we have verified to be present in nature as well. We show that, both in the model as well as in nature, the cumulative integral of aftershock magnitudes over time is a remarkable straight line with a characteristic slope. This slope is closely related to the fractal geometry of the fault surface that produces most of thee aftershocks. We also go on to discuss the implications that this feature may have in possible predictions of aftershock magnitudes or times of occurrence.

1. Introduction

Many models of natural seismicity have been proposed over the last half-decade and more. These cover a very broad range of approaches ranging from purely physical to purely statistical. The relative successes of these very diverse models is testament to the great complexity involved in the production of natural seismicity and points to the fact that the correct model is probably neither extreme and is some elusive combination of these approaches. However, an approach that has been less pursued to some extent is the investigation of the role of the fractal surface geometry of a fracture surface topography (or self affine for most natural surfaces) in producing the known statistical properties of natural seismicity. The model we propose in this article incorporates this fractal topography of the fracture surface in a simplistic way.

1.1. Earthquake statistics

The overall frequency distribution of earthquakes is given by the Gutenberg-Richter (GR) Law [1] which states

$$\log N(m) = a - bm, \tag{1.1}$$

where $N(m)$ is the frequency of earthquakes with magnitude greater than or equal to m occurring in a specified area. The parameter b, the so called b-value, has some regional variation (the value of the exponent b-value has been seen to change from one geographical region to another) but the value of b estimated from global catalogs or regional catalogs spanning many fault systems is deemed to be universal and close to unity. The constant a is a measure of the regional level of seismicity at the given lower magnitude threshold for the catalog. In particular, for aftershock sequences, the a-value points to the total aftershock productivity of the mainshock to which the sequence corresponds to. Owing to the log-linear relationship between seismic energy released and the magnitude of the earthquake, there is another form in which the Gutenberg-Richter law is stated:

$$N(\varepsilon) \sim \varepsilon^{-\alpha}, \tag{1.2}$$

where $N(\varepsilon)$ is defined in analogy to the previous form but for events which release energy greater than or equal to ε. This is due to the fact that usually magnitude is defined as logarithm of the trace amplitude on a seismogram and hence bears a log-linear relationship with energy. The temporal distribution of aftershocks of magnitude m greater than or equal to some threshold value M_c is given empirically by another well known power law, namely the Omori Law [2], saying

$$\frac{dN(t)}{dt} = \frac{1}{t^p}, m \geq M_c. \tag{1.3}$$

Here $dN(t)/dt$ gives the rate of occurrence of aftershocks at time t after the occurrence of the mainshock. The value of the exponent p is generally larger than but close to unity for tectonically active regions though a large range of variation in the p-value has been observed [3].

1.2. Modeling earthquake dynamics

The principal objective in constructing models of earthquake dynamics is to reproduce the above two empirical (statistical) laws by simulating the dynamics of a fault or of a system of interconnected faults. Different types of models have been proposed to capture this dynamics which focus on different aspects of fault dynamics. One class mimics the dynamics by slowly driving an assembly of locally connected spring-blocks over a rough surface. This essentially captures the stick slip scenario involved in generation of earthquakes. The first successful model of this kind was proposed by Burridge and Knopoff [4]. This model and all its variants [5, 6] have been reliably shown (numerically) to recreate the GR Law but the Omori Law has not been clearly demonstrated from this class of models. The underlying principle for this class of models has been found to be Self Organized Criticality [7]. There is another traditional class of

models based on the mechanical properties of deformable materials that break under a critical stress. Fiber bundle models are typical of this class.

The main class of models that we will discuss here are a relatively new type. This class of models deals with the fractal geometry of fault surfaces. We shall discuss in the next chapter some of the available observations indicating that fault surfaces are fractals and how faults are distributed in a fault zone with a fractal size-distribution. These are two very well established facts. Naturally, a few of the geometrical models of earthquakes capture the fractal effects of one fault surface sliding over the other by considering two fractals sliding over each other and by taking into account the stresses developed and released due to such overlaps. Fig. 1.1 shows a cartoon depicting this scenario. This is the basic motivation behind fractal overlap models. There have been attempts at using random fractional Brownian profiles as the fractals involved (in the so called Self-affine Asperity Model) in [8, 9]. The model yields the GR law readily and relates the b-value to the geometry of the fault. A more generalized version of the model discussed in [9] also recreates the Omori law but with a universal exponent. But in nature the exponent value varies considerably. Also, the exponent is very different in value from the exponent observed for real earthquakes (for this Self-affine Asperity Model [9] the value of the exponent is 0.37, while in nature we observe values close to unity for seismically active zones as mentioned before). Our focus though, will be on yet another geometric model which has been reasonably successful in capturing most of the observed statistical features of earthquake processes reproducing values of the parameters of these empirical laws much in agreement to what we see in nature. We call this the 'Two fractal overlap model'. The simplest scenario of a fractal sliding over its complementary set involves a Cantor set sliding over its complement. But the scenario considered here is even more simplified. We consider the overlap statistics of a Cantor set sliding over its replica. Although the model does not, to start with, consider a real fault profile the main strength of the model lies in the fact that it is completely analytically tractable and gives all the well established statistics that real earthquakes demonstrate. We will, through the length of this discussion, show these results and compare them with real earthquake data. The reader will readily recognize that these results require a knowledge of no more than high school mathematics to derive and in simplicity lies the true strength of this model.

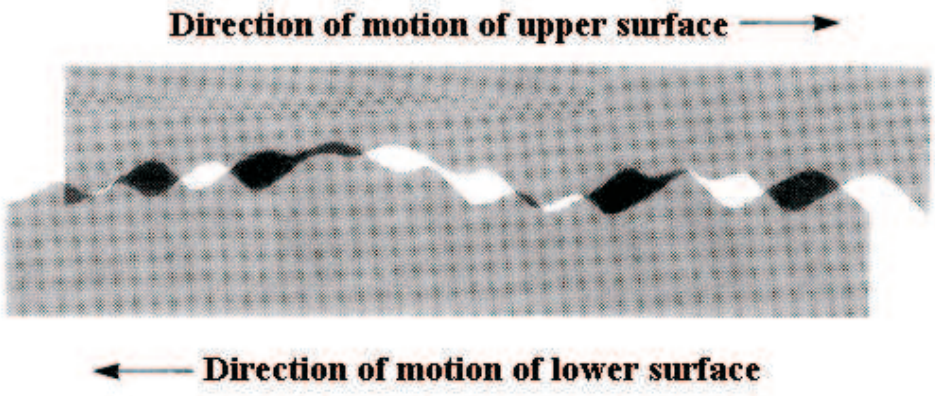

Figure 1.1: A cartoon showing overlap of two fractal surfaces. The sticking is due to interlocking of the asperities. Stress energy is accumulated and released at every slip (Adapted from [10]).

1.3. Fractal geometry of fault surfaces

Before we undertake a study and modeling of seismic activity, it is of interest to review what we imply by fractures, joints and faults. Any crack or fissure on the surface of a rock is a fracture. If the two blocks separated by the fracture are laterally displaced creating a plane across which

the rock beds are discontinuous then, in strict terms of structural geology, the locus of the discontinuity in the various rock beds is the fault. Figure 1.2 shows a fault exposure in the Dixie Valley in the United States.

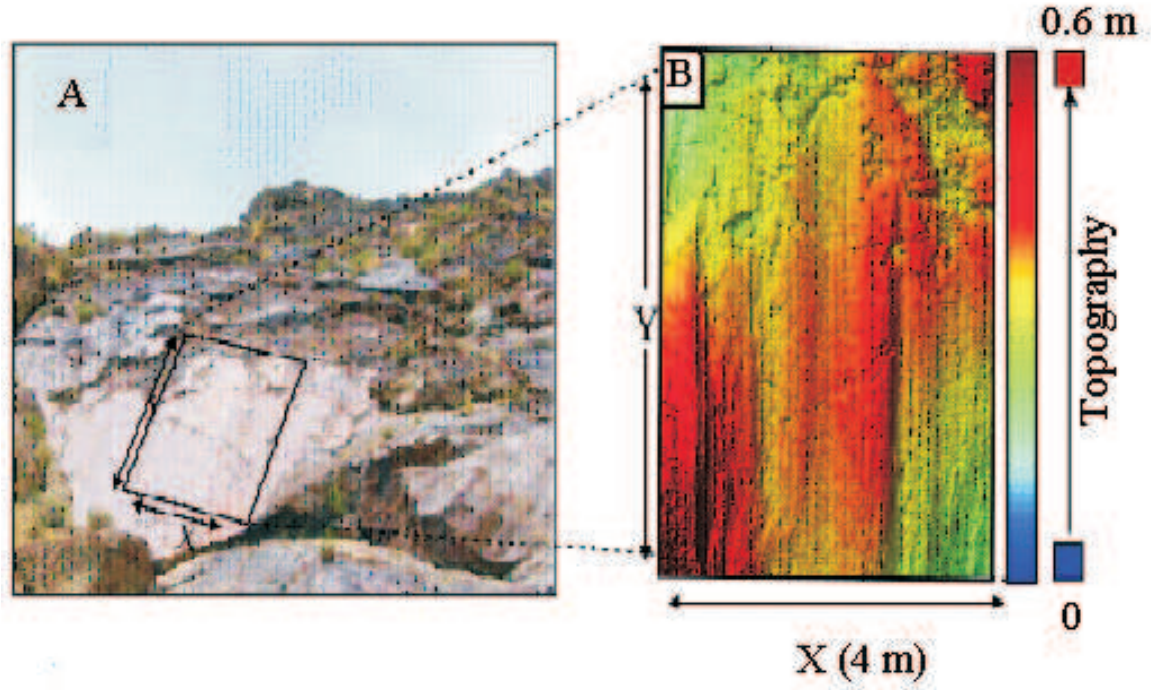

Figure 1.2: A) Chapter of a partly eroded slip surface at the Mirrors locality on the Dixie Valley fault. B) LiDAR fault surface topography as a color-scale map rotated so that the X-Y plane is the best-fit plane to the surface (Adapted from [11]).

If there has been no lateral offset across the fracture then the structure is generally referred to a joint. Faults and joints often do not come singly but in a complex system of interconnected structures. Such a system of interconnected faults is called a fault zone. In other words, it is basically a highly fractured system of fault networks all of which have been formed by the same tectonic process. It has for long been suggested that fractured rock surfaces are fractals. The fractal geometry implies a balance between two competing processes: strain weakening and strain hardening. This balance is critically tuned to produce neither positive nor negative feedback mechanisms during deformation. In such a case, the long-term deformation is accommodated statistically, at all time intervals, by structures that have no preferred size scale, i.e., structures following a scale free (due to the lack of feedback) frequency-size distribution. Fractal geometry has been reported to characterize brittle deformation structures in the crust over several bands of length scales, from regional fault networks through main traces of individual faults to the internal structure of fault zones.

In fact, fault surfaces are fractals. It was shown by [13] that the surfaces of joints are fractal. They studied the surface topography of naturally occurring joints by analyzing the power spectra of the profiles. They studied fresh joints (a fresh surface in structural geological context implies an unweathered surface) in both sedimentary and crystalline rocks, a frictional wear surface due to glacial activity and a bedding plane surface. The power spectrum of all these surfaces showed a 'red noise' spectrum over the entire spatial frequency bandwidth employed in the study with the amplitude falling off 2 to 3 orders of magnitude per decade increase in spatial frequency. This was explained using a fractal model of the topography. The dimension D was

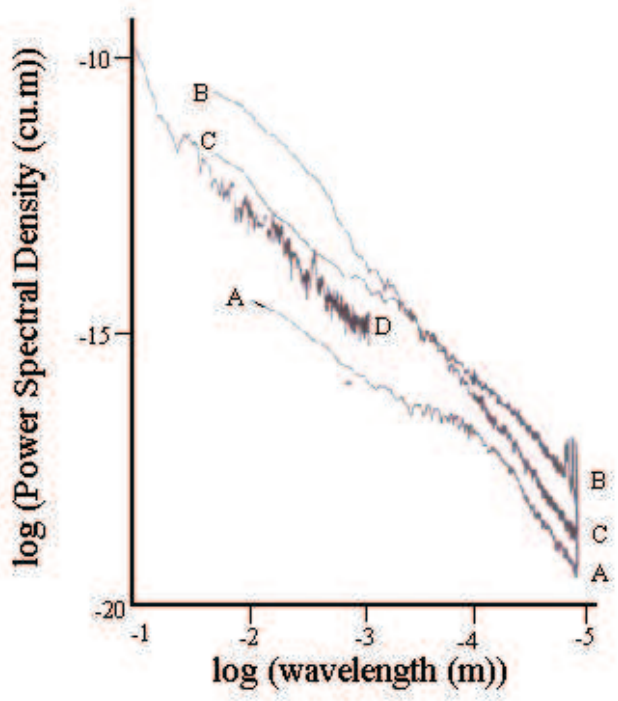

Figure 1.3: Power spectra for the fault surfaces studied in the Dixie Valley by [12]. A, B, C are from 10 – 20 mm long lab profiles. D is part of a spectrum from a 1 m long field profile. A – smoothest, unweathered hand sample of surface. B – sugary weathered surface. C – surface that apparently a is composite of sub-parallel surfaces (Adapted from [12]).

found to vary with spatial frequency. [12] did a similar analysis on the surface of faults in the western United States and found fault surfaces to be fractal over eleven orders of magnitude in wavelength. They found that the amplitude of the spectrum increased roughly in proportion to the wavelength under consideration. The power spectra for the fault surfaces in Dixie Valley (western United States) are shown in Figure 1.3 as reported in [12]. Such studies have been strengthened by modern techniques of imaging like the LiDAR profile shown in Figure 1.2. The topography of fault surfaces is now generally considered as fractal. So it is very reasonable to consider the movement of fault surfaces on and relative to one another as two fractals sliding over one another. This forms the basis of our motivation behind studying the overlap statistics of a Cantor set sliding over its replica.

2. Two Fractal Overlap model

2.1. The model

As discussed already in Section 1, earthquakes are physically caused by the slip movements of adjacent fault planes along the contact of hanging wall and footwall asperities and the release of the stress energy accumulated due to friction during the period of sticking. But as (i) faults surfaces are fractals (ii) friction is purely a surface phenomenon and (iii) the motion is, in general, in a given direction, the process that causes release of the stored elastic energy can be analyzed effectively in one dimension. Therefore a fractal embedded in one dimension can provide us a suitable geometry to investigate the overall process. The sliding of one fractal over another thus

would mimic a stick-slip scenario where the slip occurring after a stick would effectively be the physical process through which the stored energy would be released. The one dimensionality of the problem previously discussed means that we have to consider a fractal embedded in 1-D and the natural choice is a Cantor set. This is especially valid due to the fact that the projection of any fractal surface in a 1-D space is clearly a Cantor set (albeit a random one in most cases we encounter in nature). But for the sake of analytical tractability of the process we adopt, in this case, the middle third removal algorithm to generate it (fractal dimension is $\frac{\log 2}{\log 3}$). The dynamical model involves one such Cantor set moving with uniform relative velocity over its replica and one looks for the time variations of the measure of the overlapping sets common between the two at any instant of time. The model was initially given by [14]. They tackled the problem of determining the overlap statistics using a renormalization group method. We, however, present a modified analysis following [15]. This model has been extended to Sierpinski gaskets and carpets and random Cantor sets as well [16]. The model considered here however, as we said earlier, employs two regular Cantor sets of the same generation and dimension sliding over each other with uniform velocity as shown in Figure 2.1. For the n^{th} generation, the step size is $1/3^n$ and the time taken to cover each step is taken as unity. Stress energy is accumulated at each overlap of the non-empty intervals of the upper (moving) Cantor set with the non-empty intervals of the lower (stationery) Cantor set. The extent of such overlaps (the number of such overlapping non empty intervals) is represented by the 'overlap magnitude'. This measure may represent the stress (or stress energy) accumulated due to friction within the surfaces which gets released through slips. The energy released at each such 'slip' is proportional to the overlap magnitude during the 'stick' period. We therefore need to evaluate the overlap time series. At any finite generation, the time series is exactly solvable in this model.

2.2. Analysis of the time series

As mentioned already, we present here a modified version of the analysis of the Chakrabarti Stinchcombe model (or Two Fractal Overlap model) following [15]. We employ periodic boundary conditions to formulate the time series. The overlap magnitude is evaluated in terms of the number of pairs of non-empty intervals overlapping at a time. Therefore the overlap magnitude $Y_n(t)$ can only assume values in a geometric progression given by $Y_n(t) = 2^{n-k}, k = 0, 1, ..., n$. Clearly $Y_n(0) = 2^n$ and, due to the periodic boundary conditions, taking unit time to be the time required to take one step of size $1/3^n$ we obtain

$$Y_n(t) = Y_n(3^n - t), 0 \leq t \leq 3^n \tag{2.1}$$

owing to the symmetric structure of the finite generation Cantor set.

A detailed analysis of the time series reveals a straightforward recursive structure. If we simulate the overlap time series for the n^{th} generation, after 3^{n-1} time steps we have the overlap time series for the $(n-1)^{\text{th}}$ generation. Again after 3^{n-2} time steps beginning from the 3^{n-1} time steps previously taken we have the overlap time series for the $(n-2)^{\text{th}}$ generation and recursively so on. In other words the entire time series for the 1^{st} generation ($n = 1$) is contained in the time series for the 2^{nd} generation ($n = 2$) starting from the time step $t = 3$ of the 2^{nd} generation time series) and ending at the time step $t = 6$ (of the 2^{nd} generation time series). Again the entire 2^{nd} generation time series is contained in the 3^{rd} generation time series starting from the time step $t = 9$ (of the 3^{rd} generation time series) and ending at the time step $t = 18$ (of the 3^{rd} generation time series). Also the entire 1^{st} ($n = 1$) generation time series is contained in the 3^{rd} generation ($n = 3$) time series starting from the time step $t = 12$ (of the 3^{rd} generation time series) and ending at the time step $t = 15$ (of the 3^{rd} generation time series). This nested recursive structure is present throughout the time series of any n^{th} generation. Generalizing, we may state that the entire time series of the $(n-1)^{\text{th}}$ generation is contained in the time

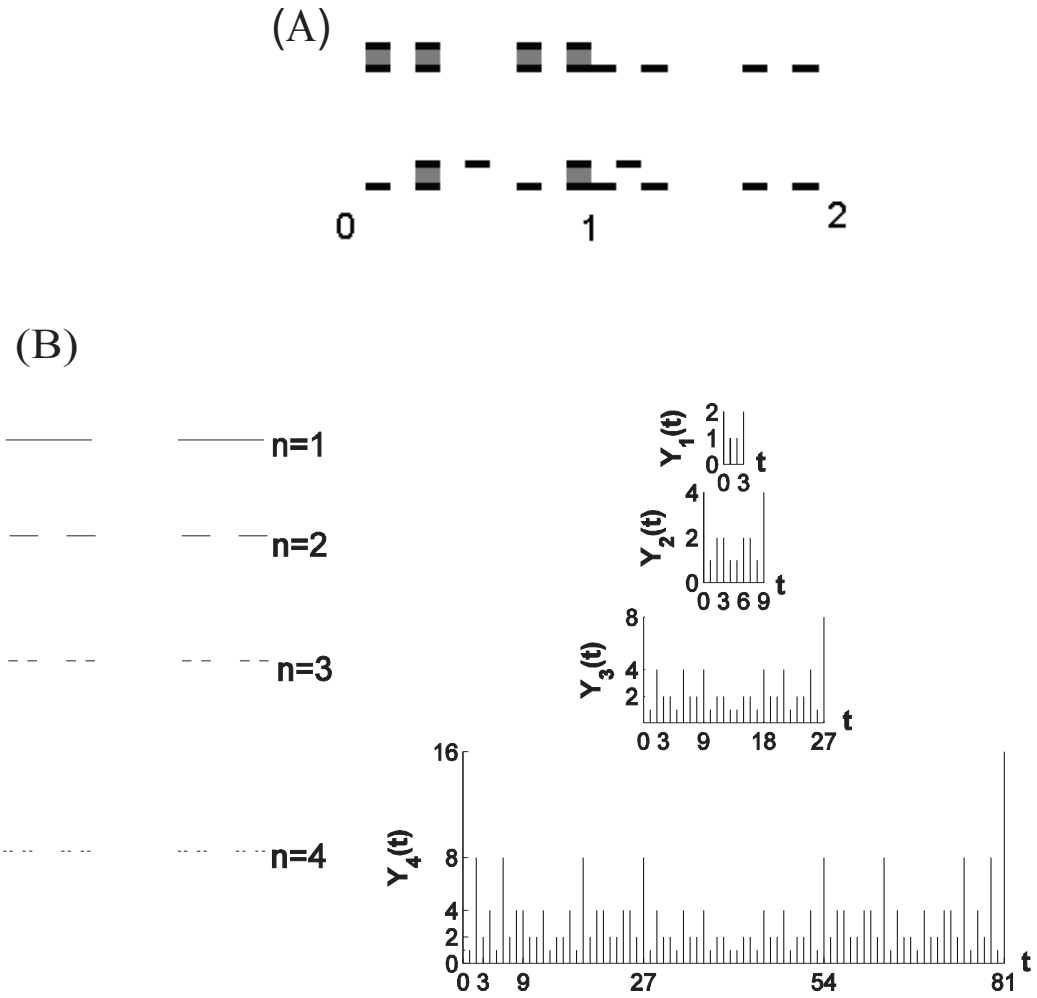

Figure 2.1: A) The recursive structure of the time series for the first four generations in the fractal-fractal overlap model. On the left the respective Cantor set generations are shown. Noticeable is the fact that the time series of all preceding generations are embedded within the time series at a given generation. B) A realization of the model for the second generation at t=0 and at t=2. The overlapping segments are shaded in grey. The lower Cantor set is repeated between 1 and 2 to employ the periodic boundary condition. The upper Cantor set slides over the lower (cf. [17]).

series of the n^{th} generation starting from the time step $t = 3^{n-1}$ (of the n^{th} generation time series) and ending at the time step $t = 2 \times 3^{n-1}$ (of the n^{th} generation time series). Again, the entire time series of the $(n-2)^{\text{th}}$ generation is contained in the time series of the n^{th} generation starting from the time step $t = 4 \times 3^{n-2}$ (of the n^{th} generation time series) and ending at the time step $t = 5 \times 3^{n-2}$ (of the n^{th} generation time series). Again, the entire time series of the $(n-3)^{\text{th}}$ generation is contained in the time series of the n^{th} generation starting from the time step $t = 13 \times 3^{n-3}$ and ending at the time step $t = 14 \times 3^{n-3}$ and so on. This can be understood very clearly from the illustrations in Figure 2.1.

There is however a finer recursive structure in the time series that leads to the analytical evolution of the number density distribution. At any given generation n, a pair of nearest line segments form a doublet and there are 2^{n-1} such doublets in the Cantor set. Within a

given doublet, each segment is two time steps away from the other segment. This means that an overlap of 2^{n-1} occurs when one of the sets is moved two time steps relative to the other. Similarly, an overlap of magnitude 2^{n-1} also occurs if one considers a quartet and a relative shift of 2×3 time steps between the two Cantor sets. Again we can consider an octet and a relative shift of 2×3^2 time steps to obtain an overlap of magnitude 2^{n-1}. In general if we consider pairs of blocks of 2^{r_1} nearest segments ($r_1 \leq n-1$), an overlap magnitude of 2^{n-1} occurs for a relative time shift of 2×3^{r_1} time steps:

$$Y_n(t = 2 \times 3^{r_1}) = 2^{n-1}; r_1 = 0, ..., n-1. \tag{2.2}$$

The complementary sequence is obtained using (2.1). We can create such rules for each of the possible overlap magnitude values $Y_n(t) = 2^{n-k}$. Rules like these give us the frequency distribution of overlap magnitudes. For example, from (2.2) we can see that as r_1 can have n possible values. Also, for each of these times at which an overlap of magnitude 2^{n-1} occurs we have another time step in the complementary sequence (due to (2.1)) at which again an overlap of magnitude 2^{n-1} occurs. Therefore the frequency of occurrence $Fr(Y_n)$ of an overlap magnitude $Y_n = 2^{n-1}$ is $2n$, that is $Fr(Y_n = 2^{n-1}) = 2n$. The complete distribution can be obtained by studying the aforementioned recursive structure carefully (the mathematical details can be found in [17]) and using simple combinatorics. The probability distribution of overlap magnitudes for the model comes out to be a binomial distribution:

$$Pr(2^{n-k}) = \begin{pmatrix} n \\ n-k \end{pmatrix} \left(\frac{1}{3}\right)^{n-k} \left(\frac{2}{3}\right)^{k} \tag{2.3}$$

where $Pr(Y_n) = \frac{Fr(Y_n)}{3^n}$, that is $Pr(Y_n)$ gives the probability of occurrence of an overlap of magnitude Y_n in a total of 3^n time steps. Now, remembering that the overlap magnitude 2^{n-k} is proportional to energy we can put $\log_2 Y_n = n - k = m$ where m is the magnitude analog for the model. It must however be kept in mind that while analyzing the model n is a constant as we are considering the model at a specific generation number and m changes as k changes. Then the frequency distribution for the model in terms of magnitude becomes

$$Pr(m) = \begin{pmatrix} n \\ m \end{pmatrix} \left(\frac{1}{3}\right)^{m} \left(\frac{2}{3}\right)^{n-m}. \tag{2.4}$$

2.3. The Gutenberg Richter law

In the limit of large n the Cantor set becomes a true mathematical fractal and we have the standard normal approximation of (2.4) which gives:

$$F(m) = \frac{3}{2\sqrt{n\pi}} \exp\left(-\frac{9}{4}\frac{(m - n/3)^2}{n}\right), \tag{2.5}$$

where $F(m)$ is the probability distribution of magnitudes $m = \log_2(Y_n)$. The objective is to show that the $\int_m^\infty F(m)dm$ gives the Gutenberg Richter (GR) law. We shall attempt to evaluate the following integral using (2.5):

$$F_{cum}(m) = \int_m^\infty F(m')dm' = \int_m^\infty \frac{3}{2\sqrt{n\pi}} \exp\left(-\frac{9}{4}\frac{(m' - n/3)^2}{n}\right) dm'. \tag{2.6}$$

This is not a standard Gaussian integral and we evaluate this integral by parts. Making the substitution $p = \frac{3(m'-n/3)}{\sqrt{2n}}$ in (2.6) we get:

$$F_{cum}(m) = \frac{3}{4\sqrt{n}} \int_{\frac{3(m-n/3)}{\sqrt{2n}}}^{\infty} \frac{2}{\sqrt{\pi}} \exp\left(\frac{-p^2}{2}\right) dp. \tag{2.7}$$

Invoking the generalized definition for the complementary error function, erfc(x), we obtain,

$$F_{cum}(m) = \frac{3}{4\sqrt{n}} \text{erfc}\left(\frac{3(m-n/3)}{2\sqrt{n}}\right). \tag{2.8}$$

For large values of the argument x, erfc(x) has the asymptotic expansion (see 7.1.23 in [18])

$$\text{erfc}(x) = \frac{\exp(-x^2)}{\sqrt{\pi}x}\left(1 + \sum_{m=1}^{\infty}(-1)^m \frac{1.3...(2m-1)}{(2x^2)^m}\right). \tag{2.9}$$

For very large x, (2.9) gives

$$\text{erfc}(x) = \frac{\exp(-x^2)}{\sqrt{\pi}x}. \tag{2.10}$$

Therefore in the limit, $m \to \infty$ we have

$$F_{cum}(m) = \frac{3}{4\sqrt{n}} \frac{\exp\left(-\frac{9}{4}\frac{(m-n/3)^2}{n}\right)}{\sqrt{\pi}\left(\frac{3(m-n/3)}{2\sqrt{n}}\right)}. \tag{2.11}$$

Equation (2.11) can be further simplified as

$$F_{cum}(m) = \frac{1}{2\sqrt{\pi}} \exp(-n/4) \exp\left(\frac{-9m^2}{4n} + \frac{3m}{2}\right)(m-n/3)^{-1}. \tag{2.12}$$

In the model, the largest value of m possible is n, therefore in the limit of large m we can assert $m^2/n \approx m$. Using the above alongwith the fact that the total number of events for a Cantor set of generation n is 3^n and $\delta m = 1$ in the model, it is easy to see that

$$\log N(m) = A - \frac{3}{4}m - \log(m - n/3), \tag{2.13}$$

where $N(m)$ is the number of earthquakes greater than a given magnitude m for the model. The term A denotes all the constants and the purely generation (n) dependent terms taken together.

Now we shall show that equation (2.13) depicts all the features of the cumulative count distribution of the model observed in simulations and seen in Figure 2.2. The third term on the right hand side shows that this form of the distribution holds only for $m \geq n/3$. For larger values of m, the linear term dominates. For smaller values of m the cumulative count becomes smaller than what is expected purely on the account of the linear term due the increasing effect of the logarithmic term. But the turning is smeared out gradually over a range of magnitudes due to the logarithmic term (as seen in the figure). The model also predicts a small bump in the cumulative statistics when the argument of the logarithmic term becomes smaller than one (due to negative values of the logarithmic term adding to the linear term). A little bit of deliberation

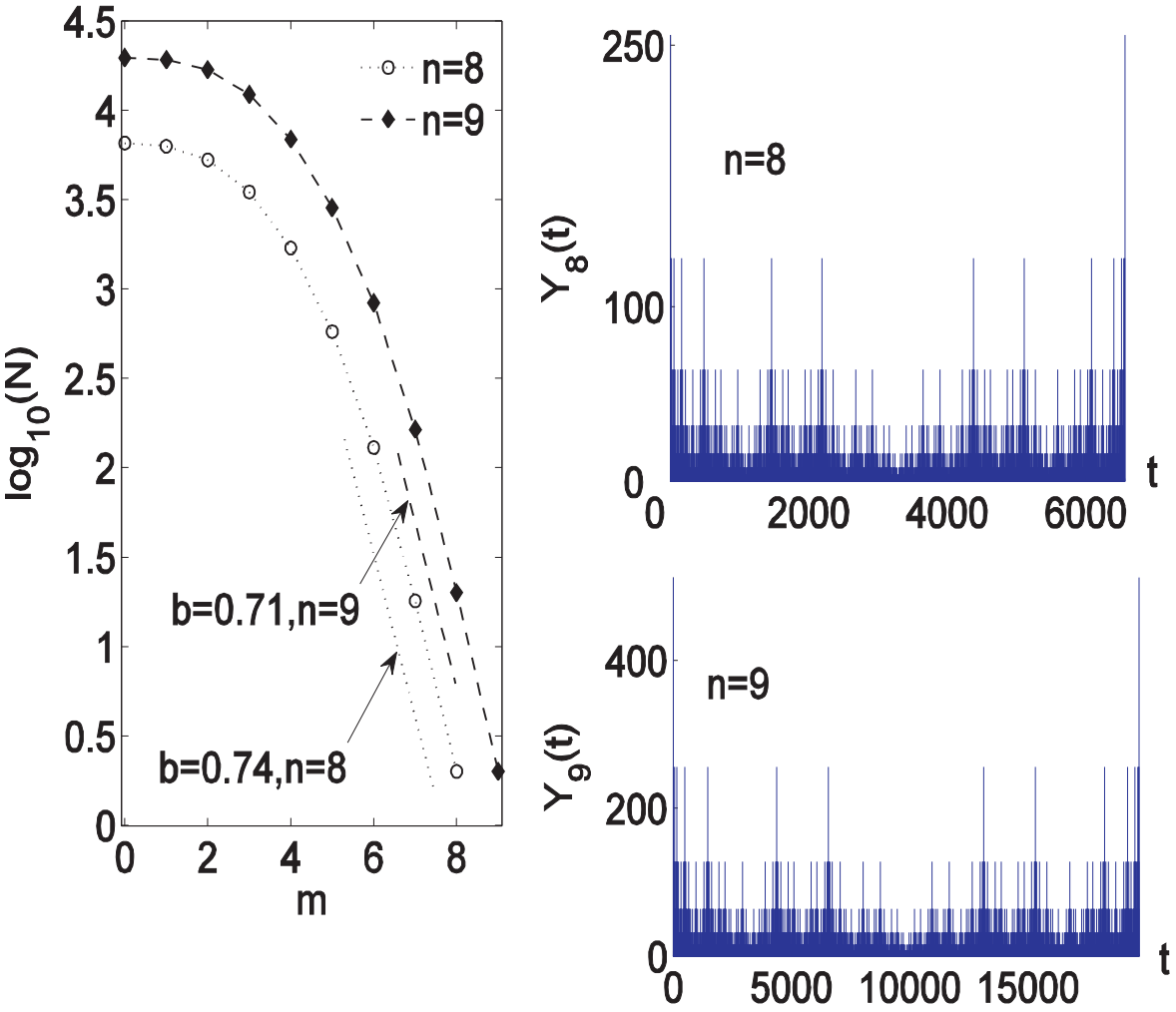

Figure 2.2: The Frequency-Magnitude (FM) plots ($\log N(m)$ vs. magnitude m, N being the number of earthquakes with magnitude greater than or equal to magnitude m) for the model for generations 8 and 9. The overlap time series are also shown on the right for the respective generations. The low-magnitude roll-off is evident for both the generations. The lines are drawn as visual aid to understand the linear trend. The b-values were obtained by fitting a linear polynomial to the data. The values of the exponents are the slopes of the indicated straight lines. The b-values thus obtained are also indicated for each of the generations (cf. [17]).

on this issue tells us that the requirement of integral magnitudes in the model does not let this condition persist for more than one magnitude value for a given value of n and even then the effect is negligible as seen from simulations. This gives the synthetic seismic sequence a smooth roll off towards the lower end of the magnitude scale. This is the precise form of the GR law as observed in earthquake seismology.

Now the so-called b-value from our theoretical distribution is 3/4 and not unity as generally reported for natural seismicity. The value 3/4 arises out of the fact that we have constructed our Cantor set by the middle third removal procedure. In fact for a Cantor set with dimension $\frac{\log(q-1)}{\log(q)}$ the exponent would be $\frac{q}{q+1}$. This of course would be effectively unity for higher

dimensional Cantor sets. Now this means that there will be region to region variation in the b-value and this is important as most other theoretical models [4, 5, 7, 19] give universal values for the exponent. In practice the b-value has shown some variability from unity. The b-value generally varies from 0.5 to 1.5 depending on the tectonic setting, tectonic stress and the magnitude ranges but normally comes close to 1 for seismically active regions [20–23]. The GR law holds good for aftershock sequences also which is really what our model describes [24, 25]. In our model however the range is from slightly smaller than 0.75 to 1 (the lower bound on the exponent is smaller than 0.75 in practice as m^2/n is slightly smaller than m in reality).

Further, the constant A in (2.13) is dependent on the generation number n and the value of n determines, for a given similarity dimension, the seismicity in our model i.e. the number of earthquakes increases with increasing n. Mathematically, A is equivalent to the constant a in the GR law. It is notable that in the GR law too a characterizes seismic activity. So A is a reasonable proxy for the a value in GR law. Figure 2.2 shows the GR law plot from the model for generations 8 and 9. The values obtained for the exponent are also indicated in the plot. The values obtained by fitting ($b = 0.74$ for $n = 8$ and $b = 0.71$ for $n = 9$) support our analysis presented above. The low magnitude roll-offs are also quite conspicuous for both $n = 8$ and 9. Comparison with the frequency-magnitude plot for Sumatra shown in later in Figure 3.1 clearly brings home the similarities between our theoretical distribution and the form observed in nature.

2.4. The Omori Law

Previously a theoretical study derived the Omori formula from a preliminary statistical model where aftershocks are produced by a random walk on a pre-existing fracture system [26]. The derived result shows a direct connection between p and the fractal dimension of the pre-existing fracture system. This study showed that the fractal properties of aftershocks are determined by the fractal geometry of the pre-existing fracture system. The Omori law comes out naturally from our fractal overlap statistics as well.

Physically, our model corresponds to an aftershock sequence for a mainshock of magnitude n. So it is of inherent interest to check for the Omori Law in our model by studying the temporal distribution of these synthetic aftershocks. The time series of overlap magnitudes in our model has built-in power law behavior. The entire magnitude-time sequence is a nested structure of geometric progressions as pointed out earlier. This makes it difficult to enumerate an exact value of the exponent p in general. But there is, however, departure from this in two limiting cases. Omori Law in practice gives specific value of p for a given magnitude threshold. We observe that for any generation, when the threshold is the minimum overlap magnitude 1 in our model, the p value is 0. This is because by the virtue of the assumption of uniform velocity there is an aftershock at every time step. A very interesting fact is however unearthed on putting the magnitude threshold at the second highest possible value $n - 1$ (that means we are considering aftershocks only of magnitude $n - 1$ and higher). Now the times of occurrences of aftershocks of magnitude $n - 1$ are at each value of $t = 2 \times 3^{r_1}$ where r_1 varies from 0 to $n - 1$. Therefore when the lower magnitude threshold is $n - 1$, we have, not considering the constant prefactor 2, consecutive aftershocks occurring at times which follow this geometric progression (2.3) with common ratio 3 (that is if at any t there is an aftershock of magnitude $n - 1$ then at $3t$ the next aftershock will occur and at 3^2t the one after that and so on). This gives the general rule $N(3t) = N(t) + 1$ leading to:

$$N(t) = \log_3 t \tag{2.14}$$

where $N(t)$ is the cumulative number of aftershocks (of magnitude $m \geq n - 1$ for a mainshock of magnitude $m = n$). To observe this, one has to remember that the symmetry in the time series is an artificially introduced artefact of the periodic boundary conditions and in the above

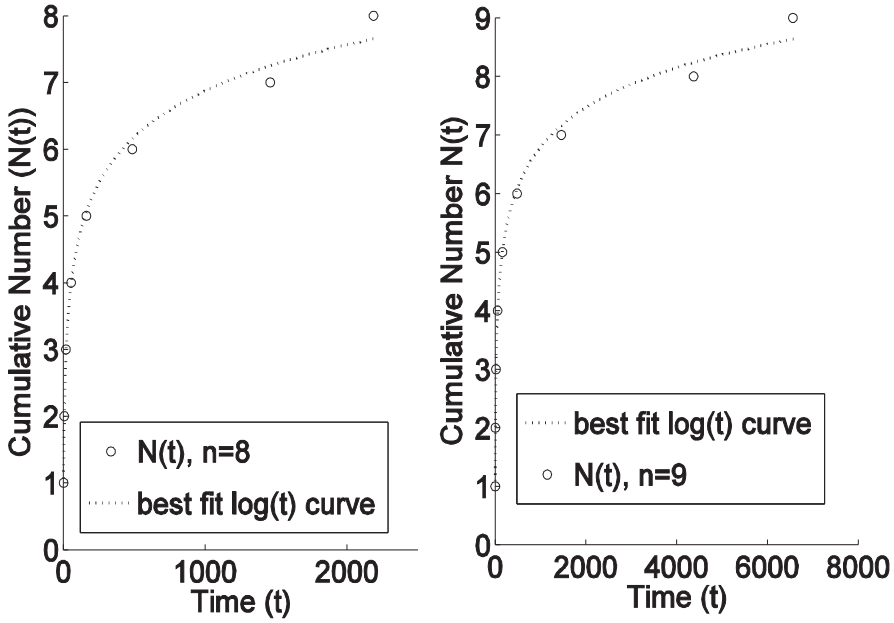

Figure 2.3: Omori Law from the model for generations 8 and 9 respectively. Dashed lines show best logarithmic fits. Plots are for $N(t)$ vs. t, $N(t)$ being cumulative number of aftershocks at time t where t is the time since the mainshock. Time parameter for the model being as defined in the text i.e. unit time for a step of size 3^{-n} (cf. [17]).

analysis we only consider the first half of the times series (e.g. see Figure 2.1). Integration of the Omori relation gives, $N(t) = 1/t^p$.

From (2.14) this gives us $p \sim 1$ which is the traditional Omori exponent value. The model therefore gives a range of p-values from 0 to 1 which systematically increases within the range with increasing threshold. Figure 2.3 shows the plots (from the model) for cumulative number of aftershocks $N(t)$ of magnitude greater than equal to $n-1$ versus t for $n = 8$ and $n = 9$.

The fact that the Omori exponent p is not universally unity is a very well documented fact and some workers have reported variability in p from 0.5 to 2.5 [27]. But for seismically active zones p is generally larger than but close to unity. This variability is present in our model too. The variability in p in our model apparently stems from implementing different magnitude thresholds.

But, there is a more subtle feature of this analogy with the real world. The magnitude threshold for Omori Law calculations is always put above the completeness magnitude M_c. Completeness magnitude is that magnitude below which the frequency-magnitude statistic rolls-off from the GR like power law. It is generally believed that the number of earthquakes is not exhaustively recorded below this magnitude and this is the reason for the roll-off [28, 29]. In other words the complete record of earthquakes below this magnitude is not available in the sense that the frequency level below this magnitude is less than what really should be according to the GR law. For real earthquakes Omori Law exponents are calculated only in the power law region of the magnitude scale. In our model such a roll off occurs naturally. The roll-off occurs at approximately below a magnitude $n/3$ as discussed in Section 2.3. A meaningful comparison with the Omori statistics for real data sets can be done only for the power law region and that means our threshold can be no smaller than $n/3$. This implies that the p-value can never be observed to be zero. And for a higher generation or a higher dimension fractal, at the same magnitude cut-off, the p exponent will be higher than a lower dimension or lower generation

fractal. Values of p closer to unity will be seen as we take up Cantor sets of progressively higher dimensions and/or generations at the magnitude cut-off $n/3$. The higher the generation and/or dimension of the fractal we consider the higher will be the mainshock magnitude and more number of aftershocks will be observed in the model. Thus the seismic activity will increase. At the same time the exponent p will yield values closer to unity even at magnitude cut-offs lower than $m = n - 1$. Thus for seismically active zones p-values will be closer to unity. One might be tempted to extend this analogy to real seismicity and conclude that the p-value is close to 1 as observed in seismically active regions. This would be far-fetched as the p-value is generally observed to be larger than and nearly equal to unity for seismically active regions. Our model approaches 1 from the left hand side on the real number line and hence the analogy is not very direct in terms of the values of the exponent. But the analogy of the form of the temporal decay is direct and unmistakeable and shows that the Omori Law behavior might also be linked to the fractal geometry of the fault.

2.5. Temporal distribution of magnitudes of an aftershock sequence

There is another very important observation that comes out from the model. If we evaluate the time cumulant of magnitude, i.e. $\int_0^t m(t')dt'$ where t is the time since the mainshock and $m(t)$ is the magnitude at t, it comes out to be a remarkable straight line. In other words:

$$Q(t) = \int_0^t m(t')dt' = St \tag{2.15}$$

where S is the slope of the straight line. This temporal distribution of the $Q(t)$ statistic is very significant. The slope S is a function of both the generation number as well as the dimensionality of the Cantor set. It is however quite difficult to enumerate the slope exactly due to the presence of the nested geometric progressions in the time series as stated earlier but an approximate estimate of the slope is given by

$$S_n^q = \left(\frac{q-1}{q}\right)\frac{n}{2} \tag{2.16}$$

for the model where the Cantor set has been formed by removing the middle block from q blocks and the generation number is n. Now the important fact coming out of (2.16) is the dependence of S on both the dimension and the generation number of the model. The model predicts that the slope S for real aftershock sequences would be fault dependent as we expect the generation number and/or the dimension of the fractals involved to vary from fault to fault. Thus in a sense, the slope S is a kind of a 'fractal fingerprint' of the fault zone. The slope is a very characteristic local feature of the aftershock sequence and hence of particular interest as a diagnostic feature of aftershock sequences. In effect this provides us a new approach in analyzing the temporal behavior of aftershock sequences from which we can, at least from the model, clearly extract information about the fault geometry. The precise meaning of the slope comes out to be something a bit different when we put the value of q into (2.16) for the middle third removed Cantor set we have used here. Here $q = 3$ giving the slope to be equal to approximately $n/3$.

A look back at (2.5) immediately brings home the meaning of the slope. It is simply the average magnitude of the Gaussian distribution of the aftershock magnitudes generated by the model. The significance of this will become even more clear when we look for this feature of aftershock statistics in real earthquakes. Let us suspend this discussion for then and look at Figure 2.4 for such $Q(t)$ vs t plots for the model for $n = 7, 8, 9$ respectively. From the figure one can clearly see the increase in slope with successive increases in generation number n. The increase in generation number is something that we might expect in an active seismic zone. This can take place due to re-rupturing of an existing rupture zone. Such re-rupturing has been

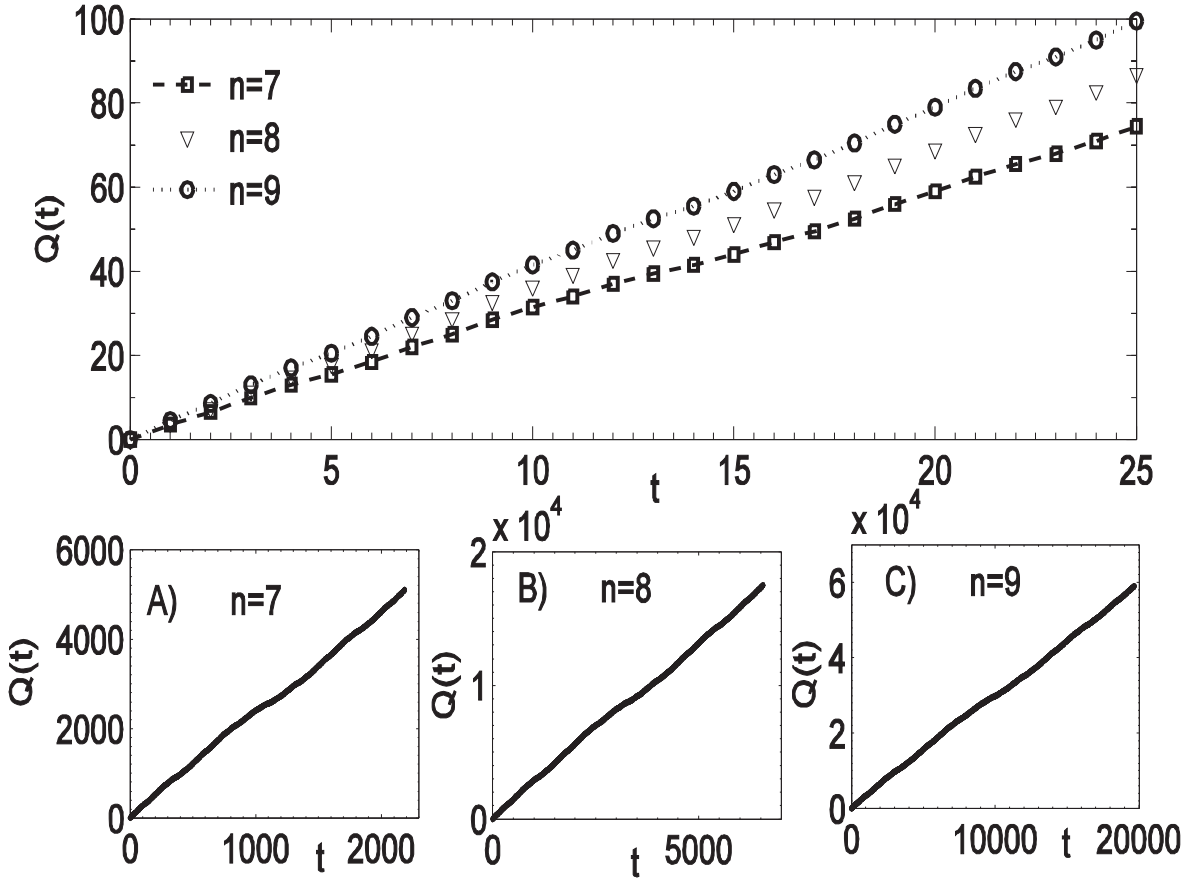

Figure 2.4: The $Q(t)$ vs. t statistic for the model for generations 7, 8 and 9. At the top plots for all the three generations (for the first 25 time steps) are shown together to show the increase in slope with increase in generation number n. At the bottom plots A), B) and C) show the entire $Q(t)$ time series for generations 7, 8 and 9 respectively (cf. [17]).

reported very often and happens when an earthquake occurs at or near the hypocenter of a previous large earthquake (hypocenter is the assumed point from which seismic waves emanate) years afterwards. We discuss such an event and the resultant $Q(t)$ vs. t plot in Section 3.3.

3. Comparison with observations

3.1. The Gutenberg Richter law

In Figure 3.1 we have considered the frequency-magnitude distribution for two real aftershock sequences to compare our theoretical formulation (see Section 2.3) with real earthquake data. The data sets considered were 1) The 2004 Sumatra earthquake aftershock sequence (26/12/2004, $M_w = 9.0$, Epicenter latitude: 3.30°, Epicenter longitude: 95.98°, source catalog: NEIC (PDE) catalog (`http://neic.usgs.gov/neis/epic/`) and 2) The 1995 Kobe earthquake aftershock sequence (17/01/1995, $M_{JMA} = 7.2$, Epicenter latitude: 34.6°, Epicenter longitude: 135.0°, source catalog: JUNEC catalog (`http://www.eic.eri.u-tokyo.ac.jp/CATALOG/junec/monthly.html`). Aftershocks of a major event were considered to be events within a given region, geographically defined as boxes or polygons constrained by suitable latitudes and longitudes, and the magnitudes were recorded over a length of time (of the order of a year or more) over which the region has not yet relaxed to its background seismicity

(tentatively within the first 1000 days). Now one point needs to be made clear with respect to the Sumatra dataset. The dataset was inhomogeneous in the sense that it reported earthquake magnitudes in different magnitude units. So we had to convert all the magnitudes reported to one uniform magnitude scale using inter-magnitude conversion relationships. We chose the uniform magnitude scale for our work to be the moment magnitude M_w as defined in [30]. For the Sumatra event we used the conversion relationships used in [31]. These relationships were specifically designed for the aftershock sequence of the Sumatra event extracted from the PDE catalog and hence serve our purpose. The fact that the conversion relationships were designed for nearly the same dataset as we have used here is important as such conversion models are in general regressional models and hence their use in our work is validated by the fact that here we use them on the same population for which they were originally designed. But errors in magnitude reporting as well as those induced due to magnitude conversions can severely affect the estimation of the GR law exponent. These errors have been discussed in a bit more detail in Section 3.3.

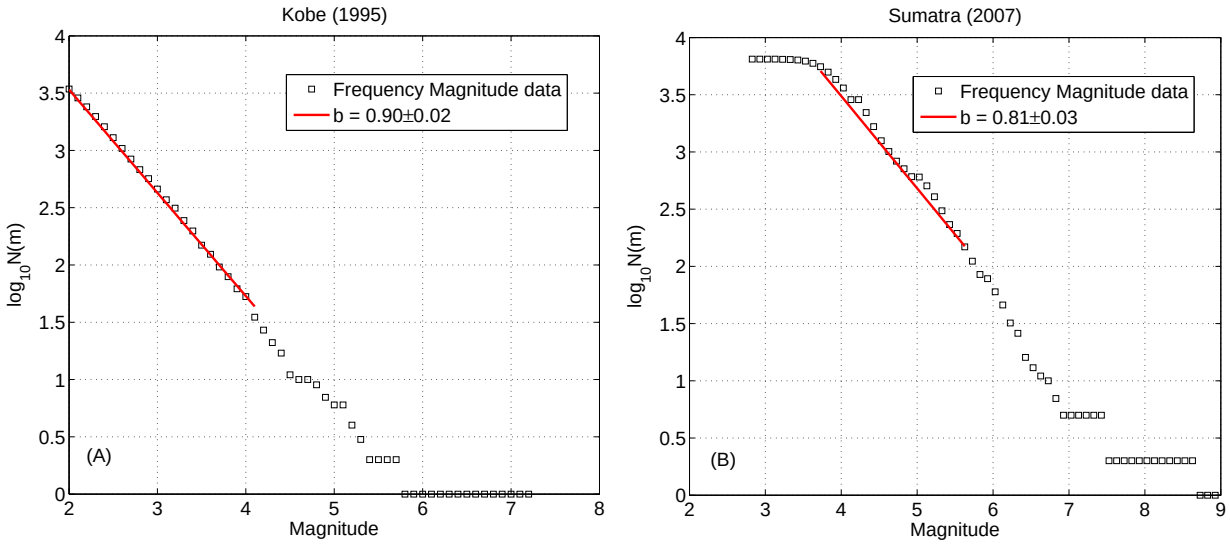

Figure 3.1: GR or Frequency-Magnitude distributions for the aftershock sequences described in the text A) the 1995 Kobe earthquake and B) the 2004 Sumatra earthquake. We clearly see the lower magnitude roll-off from the power law distribution in Sumatra. $N(m)$ represents number of earthquakes with magnitude greater than or equal to m, m represents magnitude.

As we remarked earlier, the frequency-magnitude plot for the Sumatra aftershock sequence clearly shows the roll off from GR statistics at the low magnitude end. This is similar visually to the roll off observed in our model (see Section 2.3 and Figure 2.2). But the Kobe sequence does not show any such clear roll-off. According to conventional wisdom in statistical seismology, this means that the Kobe sequence is probably complete upto $m = 2.0$. According to the model however, this means that the instrumentation deployed by the network only records events larger than the physical roll-off threshold. As the JUNEC catalog is well known for its accuracy, one might assume that this means that the threshold itself is low or the fault is of small generation number. The roll-off phenomenon will be observed again when we present the GR plots for the various aftershock sequences used in Section 3.3.

3.2. The Omori law

Our model shows that the Omori exponent p (see equation (1.3)) increases with increase in the lower magnitude threshold. We tried to check for this trend of increase in p with increase in lower magnitude threshold for three real aftershock data sets. The aftershock sequences chosen were 1) 1989 Loma Prieta earthquake aftershock sequence (18/10/1989, M_w= 7.1, Epicenter latitude: 37.0°, Epicenter longitude: -121.88°, source catalog: same dataset as [32]); 2) 1999 Chamoli earthquake aftershock sequence (29/03/1999, M = 6.6, Epicenter latitude: 30.51°, Epicenter longitude: 79.40°, source catalog: Wadia Institute of Himalayan Geology catalog (same dataset was used in [33]) and 3) 2004 Sumatra earthquake aftershock sequence described before. The results are given as $\log n(t)$ vs. $\log t$ plots in Figure 3.2 where the cut-off thresholds are denoted as M_c and the p values are indicated. Here $n(t)$ denotes number of aftershocks per unit time and t denotes time since the mainshock in days. As is evident from Figure 3.2, the increase in p with increase in M_c is clearly seen in Chamoli and in Sumatra. However in Loma Prieta, which is a very well characterized data set, the same trend is not seen. The reason for widely different values of M_c for the three data sets is that the completeness level (as explained earlier meaningful analysis can only be done above the completeness magnitude) for the three catalogs are very much different mainly due to the nature of the seismic networks implemented.

Most statistical seismologists now agree that the Omori law is too simplistic a model to describe the true nature of the temporal decay of aftershock sequences. It is now standard to describe the decay of aftershock rates by the more complicated modified Omori law [3]

$$\frac{dN}{dt} = \frac{1}{\tau[1 + t/c]^p}, m \geq M_c \tag{3.1}$$

where t is time elapsed since the mainshock, M_c is a lower magnitude cutoff above which earthquakes are taken into account, τ and c are characteristic times, and p is an exponent specifying how fast the sequence is decaying in time. The mechanism behind the time dependence in Omori law has been debated. Elastic effects work on short time scales and cannot explain the gradual decay of aftershock sequences over very long times. Therefore, the value p is thought to reflect the mechanical conditions of Earth's crust. There have been reports of systematic regional variations of the p-value in Japan which could be attributed to regional variation of surface heat-flow values [27, 34]. The central argument behind this hypothesis is that aftershock activity decays faster as the stress relaxes faster in regions of higher crustal temperature. Many other mechanisms have been proposed for this temporal decay e.g. subcritical crack growth [35], visco-elastic relaxation [36], post-seismic creep due to stress corrosion in the regions of stress concentration after the mainshock [37], static fatigue [38], pore fluid flow [39], post-seismic slip [40] and earthquake nucleation under rate- and state-variable friction [41]. In general, it is assumed that the parameters c and τ are constants and are specific to a given aftershock sequence. The significance of the parameter c has been somewhat debated. It may reflect the poor detection level during the early post-seismic period when coda waves from the mainshock make it difficult to identify aftershocks or large magnitude event swarms mask smaller events [38, 42]. It may have more physical connotations as well; e.g. due to finite duration of earthquake nucleation time [35, 41] or, for post-mainshock seismicity driven by afterslip, due to the response of aseismically creeping zones to the co-seismic stress change [43]. It recently has been suggested that τ and c may be considered functions of the lower magnitude cutoff M_c, and thus may be written as $\tau(M_c)$ and $c(M_c)$ [44]. In view of this discussion, it must be recognized that our model does not capture the modified Omori Law. Hence the analogy of the behavior of the p-value in the model with that in nature is very approximate at best in the physical sense and is only valid if one accepts the Omori Law decay of aftershocks rather than the modified Omori Law decay as the mathematical description of the temporal decay of aftershock rate.

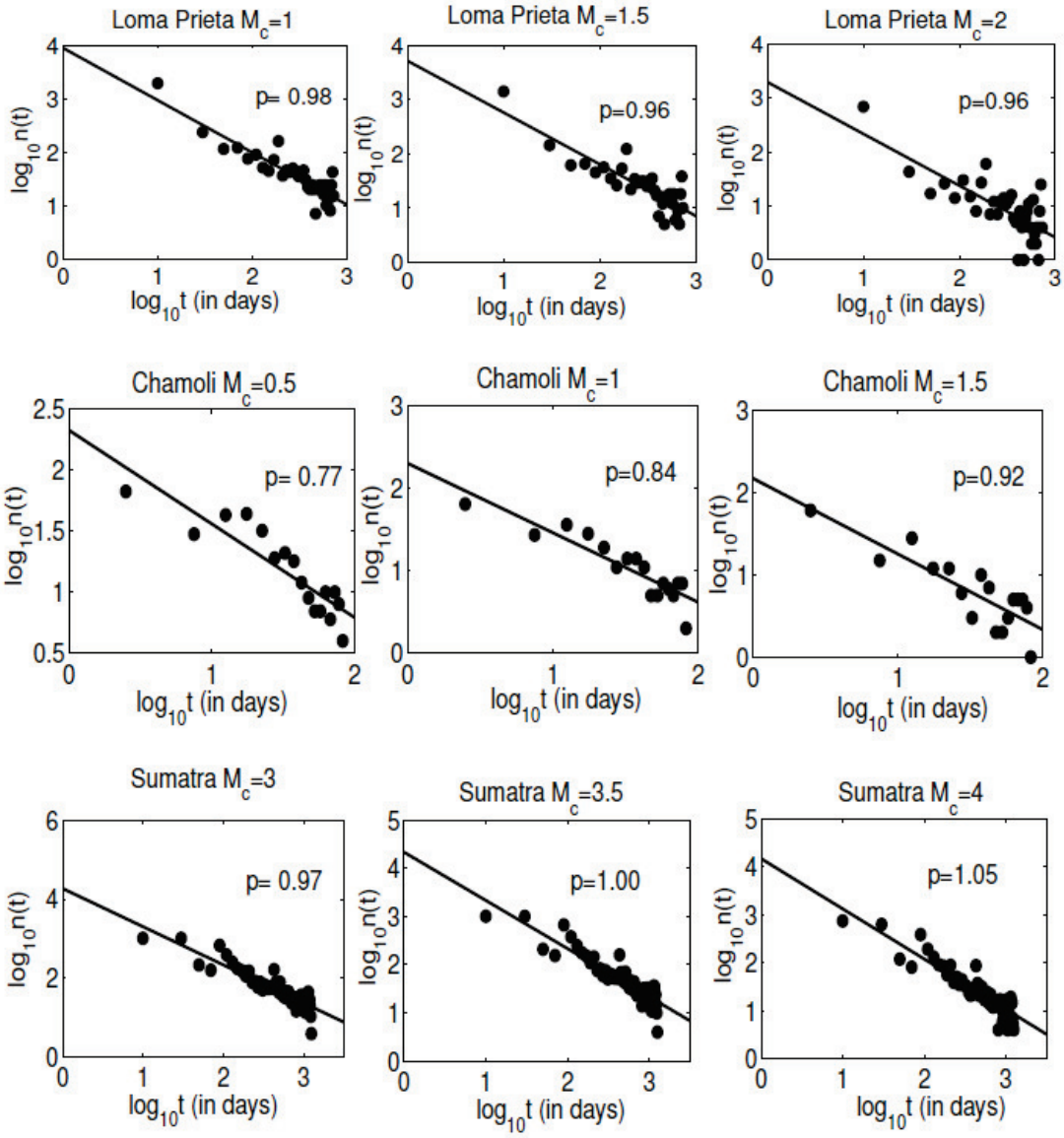

Figure 3.2: The plots for number of aftershocks per unit time $n(t)$ vs. time since the mainshock in days, t, for the Loma Prieta, Chamoli and Sumatra data sets. The cut-off magnitudes M_c are indicated in each plot title. The corresponding p values are shown within the plots. The solid lines give the linear fits to the data with slope p (cf. [17]).

3.3. The temporal distribution of aftershock magnitudes

To establish the observations obtained for the $Q(t)$ statistic. We first collected the aftershock magnitude-time sequences $m(t)$ of eleven major earthquakes from different geographical regions of the world. The earthquakes were selected carefully from all over the globe to ensure that no regional bias was introduced due to the choice of a specific catalog or a specific geological setting. We also intentionally selected some multiple events in the same geological region on a) different fault zones b) the same fault zone at a different time. We then evaluated a cumulative

integral $Q(t)$ of the aftershock magnitudes over time. Numerically, we evaluated the integral $Q(t) = \int_0^t m(t')dt'$, the time cumulant of magnitude where t denotes the time since the main shock. The integration is done over all event magnitudes above a threshold level, in this case chosen to be the completeness magnitude M_c. The datasets we used for our analyses are as follows (some of the datasets used here have already been cited in Sections 3.1 and 3.2 and used for calculations and we restate them again for the sake of completeness):

a) The 1989 Loma Prieta earthquake (18/10/1989, M_w = 7.1, 37.0°, - 121.88°). The data set used was the same as the one used in Section 3.2.

b) The 1995 Kobe earthquake (17/01/1995, M_{JMA} = 7.2, 34.6°, 135.0°). The aftershock region was chosen on the basis of the work of [45] (latitudes 34°-36°, longitudes 133.5°-137°). The data were taken from the JUNEC catalog (`http://www.eic.eri.u-tokyo.ac.jp/CATALOG/junec/monthly.html`) for the period 17/01/1995-31/12/1995.

c) The 2004 Sumatra earthquake (26/12/2004, M_w= 9.0, 3.30°, 95.98°). The box was chosen in accordance to the earthquake summary poster prepared by the USGS (available at `http://earthquake.usgs.gov/eqcenter/eqarchives/poster`). The box chosen was latitudes 0°-20°, longitudes 90°-100°. The data were taken from the NEIC (PDE) catalog (`http://neic.usgs.gov/neis/epic/`) for the period 26/12/2004-28/05/2008.

d) The 2005 Muzaffarabad (Kashmir, North India) earthquake (08/10/2005, M_s= 7.7, 34.52°, 73.58°). The box chosen is defined by latitudes 33.5°-35.5° and longitudes 72.2°-74.2°. The data were once again from the NEIC (PDE) catalog (`http://neic.usgs.gov/neis/epic/`) for the period 08/10/2005-28/02/2008.

e) The 1999 Chamoli earthquake (29/03/1999, M_s = 6.6, 30.51°, 79.40°), the aftershocks were obtained from a highly localized network employed by the Wadia Institute of Himalayan Geology (same dataset as used in [33]).

f) The 2003 Bam earthquake (26/12/2003, M_s = 6.8, 29.00°, 58.31°).The box was chosen to be latitudes 27.5°-30.5° and longitudes 57.5°-59.5°, the time interval being from 26/12/2003-26/12/2005 on the IIEES listing (`http://www.iiees.ac.ir/iiees/EQsearch/(4tswcof3bokb2r2z0gca4245)/EventQuery.aspx`) reported only in local magnitude M_L.

g) The 2005 Zarand earthquake (22/02/2005, M_s = 6.5, 30.80°, 56.76°), the aftershock sequence was chosen over latitude extent 29.5°-32.5° and longitude extent 55.5°-59.5° for the time period 22/02/2005-22/02/2007. The catalog used was again IIEES (`http://www.iiees.ac.ir/iiees/EQsearch/(4tswcof3bokb2r2z0gca4245)/EventQuery.aspx`).

h) The 2002 Denali fault earthquake in central Alaska (03/11/2002, M_S=8.5, 63.52°, -147.44°). The listing was taken from the NEIC (PDE) listing (`http://neic.usgs.gov/neis/epic/`). The box was: latitude 65.0°-60.0° and longitude -141.0°-(-151.0°) and the time window was 23/10/2002-02/05/2008. This sequence is referred to as Alaska 1 henceforth in the text.

i) The 2003 Rat Islands, Aleutian Islands earthquake in Alaska (17/11/2003, M_w = 7.8, 51.15°, 178.65°). The source was again the NEIC (PDE) catalog (`http://neic.usgs.gov/neis/epic/`). The latitude longitude box was defined by latitudes 54°-50° and longitudes 174°-(-174°) and the time series was taken between 17/11/2003-02/05/2008. This dataset is henceforth referred to as Alaska 2.

j) The 2002 Taiwan earthquake (31/03/2002, M_w = 7.1, 24.13°, 121.19°) for which the listing was taken from BATS (Broadband Array in Taiwan for Seismology) CMT catalog (`http://tecws.earth.sinica.edu.tw/BATS/cmtbyform.php`). The relevant box was latitudes 20°-23° and longitudes 119°-122° for the time period 31/03/2002-31/03/2005. This sequence is called Taiwan 1 in the text.

k) Another 2006 Taiwan earthquake on the same plate boundary, viz. the Eurasian plate and the Philippines plates, (26/12/2006, $M_w = 6.7$, 21.89°, 120.56°). The latitude longitude box was defined as 20°-23° and 119°-122° and the time window was 26/12/2006-23/05/2008. The catalog was once again the BATS CMT catalog (`http://tecws.earth.sinica.edu.tw/BATS/cmtbyform.php`).

(All dates are expressed as dd/mm/yyyy, positive latitude implies northern hemisphere, positive longitude implies eastern hemisphere, negative latitude implies southern hemisphere and negative longitude implies western hemisphere.) The spatial distribution of aftershocks for each of these sequences is shown in Figure 3.3. $Q(t)$ for each of the above aftershock sequences was estimated using numerical integration.

The important limitation of our analysis, while evaluating the aforementioned integrals, is the fact that more often than not most catalogs which give the most exhaustive list of aftershocks report the various events in different magnitude scales. This warrants the need for using conversion relationships to convert the various magnitude scales to a uniform scale. This, wherever we have inhomogeneous catalogs, we have chosen to be M_w, the moment magnitude as defined by [30] analogous to the previous sections. To this end we have used well defined and previously employed conversion relationships. The datasets extracted from the NEIC (PDE) catalog are all inhomogeneous with respect to the magnitude scales used to report the various events.

The PDE listing was used in cases of the Sumatra, Muzaffarabad and the Alaska events (see Table 3.1). For the Sumatra event we used the conversion relationships used in Section 3.1. These relationships were specifically designed for the aftershock sequence of the Sumatra event extracted from the PDE catalog and hence serve our purpose. For the Muzaffarabad event we used conversion relations given in [46] which were again designed specifically for the region and is based on the PDE listing. The fact that the conversion relationships were designed for nearly the same datasets as we have used here is important as such conversion models are in general regressional models and hence their use in our work is validated by the fact that here we use them on the same Alaska 1 and Alaska 2 we could not obtain valid conversion relationships. Our strategy for these two sequences is described later in the text. Once we had homogeneous magnitude-time listings, we calculated the b-values and completeness magnitudes (M_c) for each of the recorded aftershock sequence. Our estimate of M_c is based on the assumption that the GR law [1] explains a large percentage of the frequency-magnitude distribution above a given completeness magnitude. We assumed the percentage to be an ad hoc 90% and followed the methodology in [28].

It has been recently noted [29] that the assignment of a single completeness magnitude to an aftershock sequence is oversimplified and the M_c for such sequences have temporal variability. Within the first hours to days of an aftershock sequence, M_c tends to decrease systematically. This is caused by improvements of the station network and the fact that the frequent larger aftershocks eclipse smaller events. In our case however, as we track an aftershock sequence over a large period of time exceeding at least a year, this initial variability has been disregarded and a unique M_c has been ascribed to each of the homogenized sequences. Such an assignment is problematic for the Alaska 1 sequence due to the lack of homogeneity (and hence increased possibility of bias in determination of the b-value) discussed previously. So we progressed following a different methodology. For Alaska 1, the most numerous listing of events was in M_L. So we chose this subset of the data (1848 events out of a total 2031 events) and calculated the b-value and M_c on this set. This was done keeping in mind that the lower magnitudes are more regularly reported in M_L in the PDE catalog.

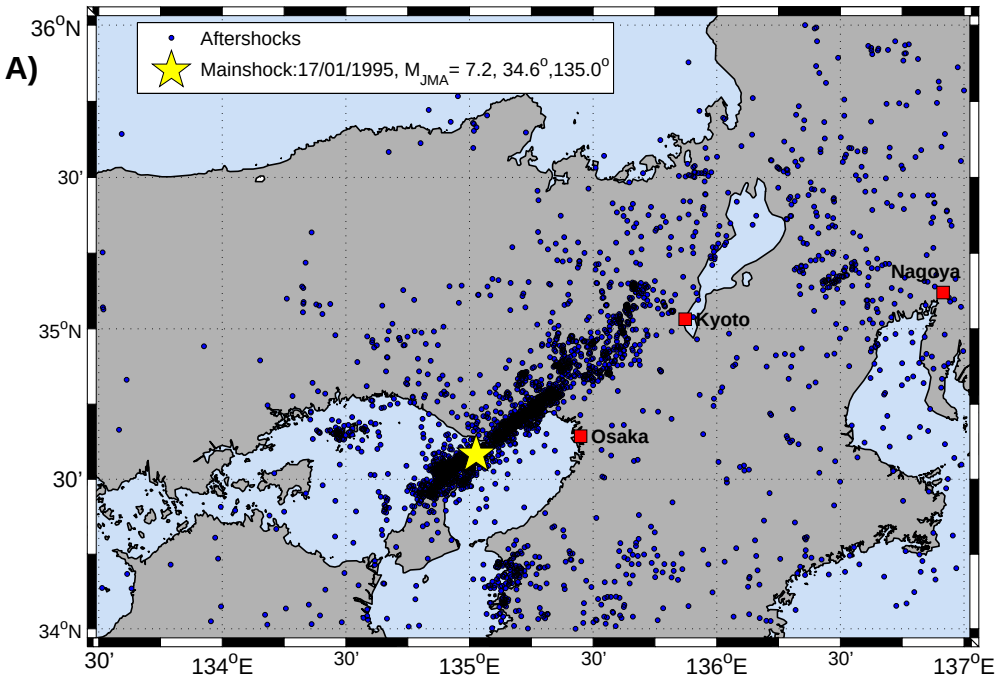

(a)

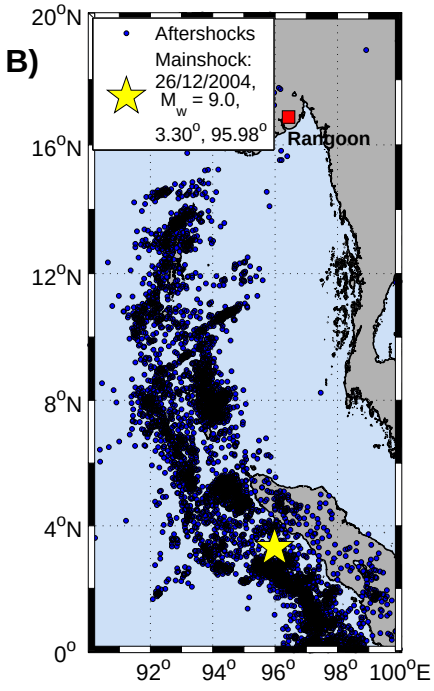

(b)

Figure 3.3: Maps showing spatial distribution of aftershocks chosen for A) Kobe, B) Sumatra datasets.

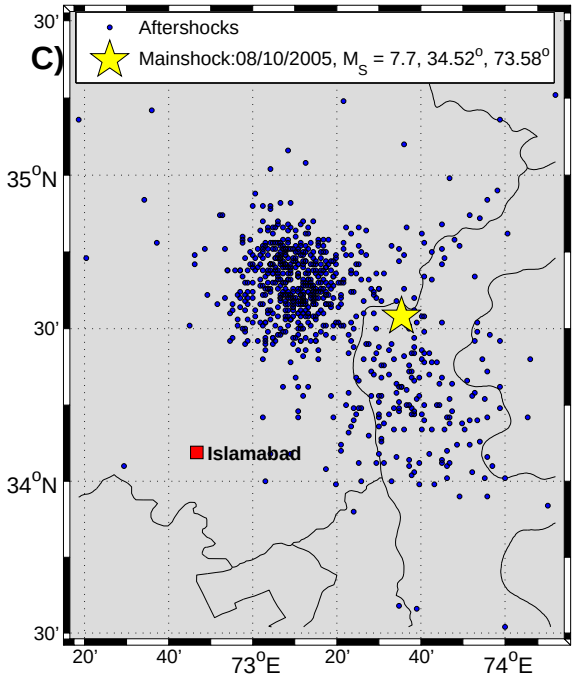

(c)

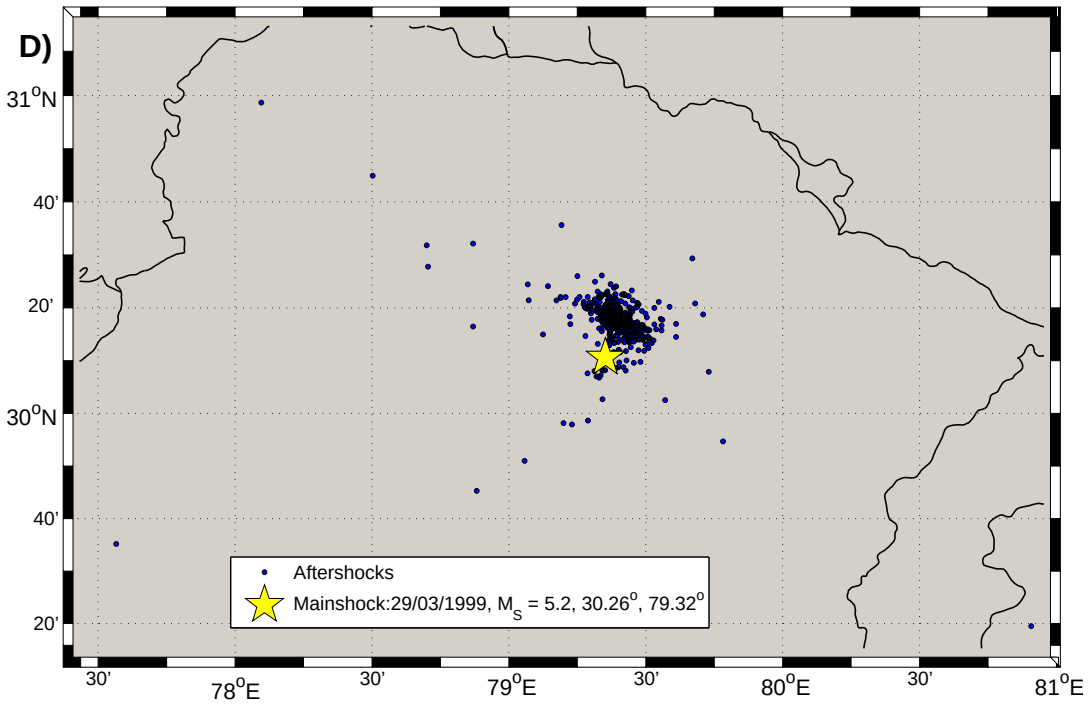

(d)

Figure 3.3: Maps showing spatial distribution of aftershocks chosen for C) Muzaffarabad, D) Chamoli datasets.

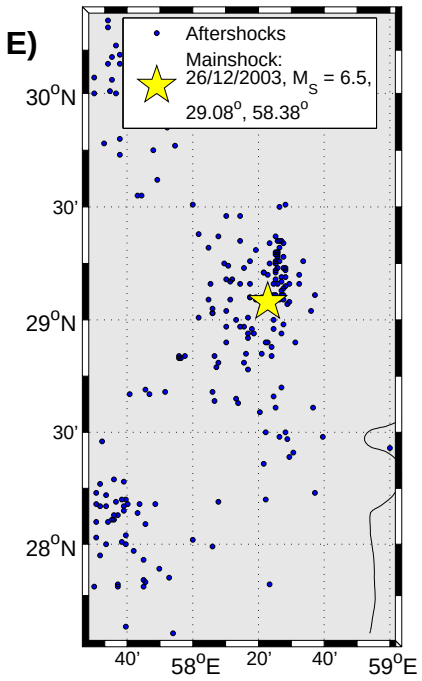

(e)

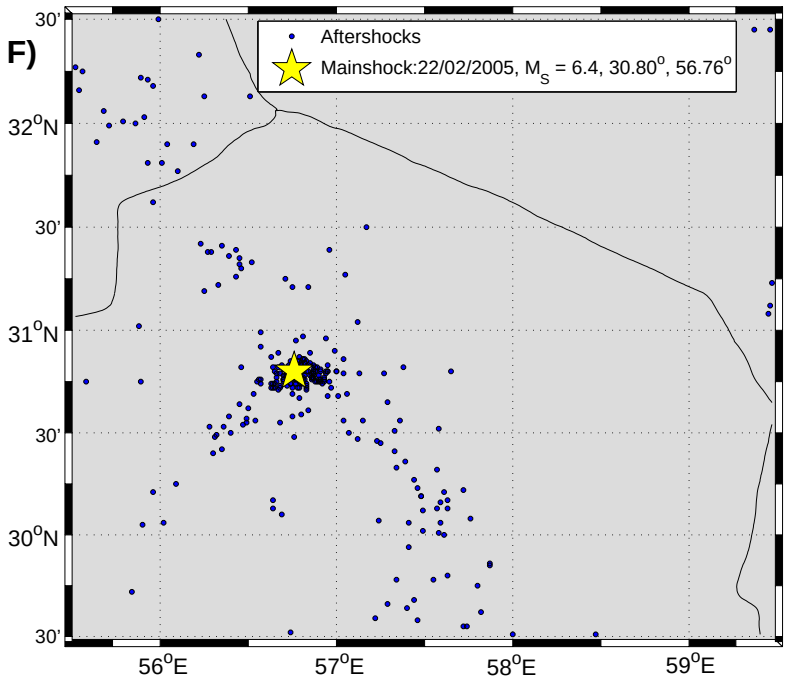

(f)

Figure 3.3: Maps showing spatial distribution of aftershocks chosen for E) Bam, F) Zarand datasets.

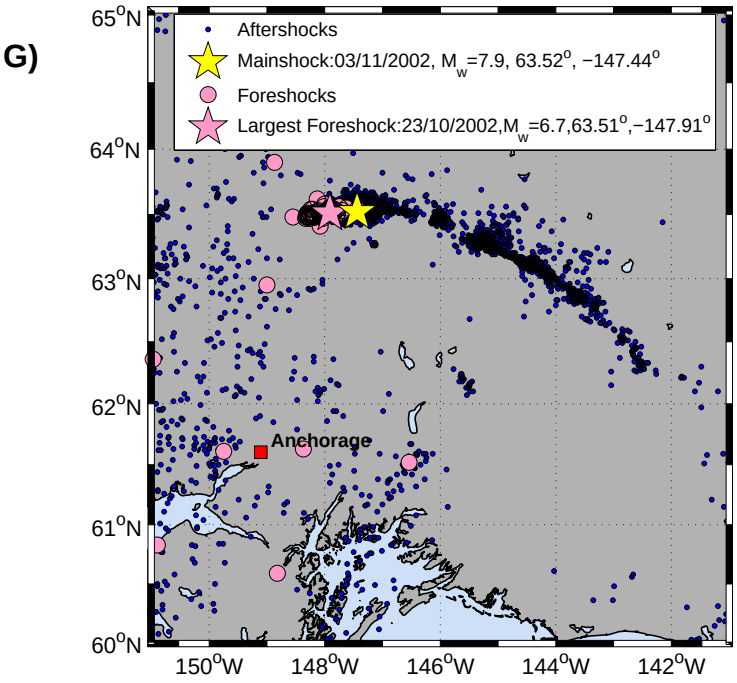

(g)

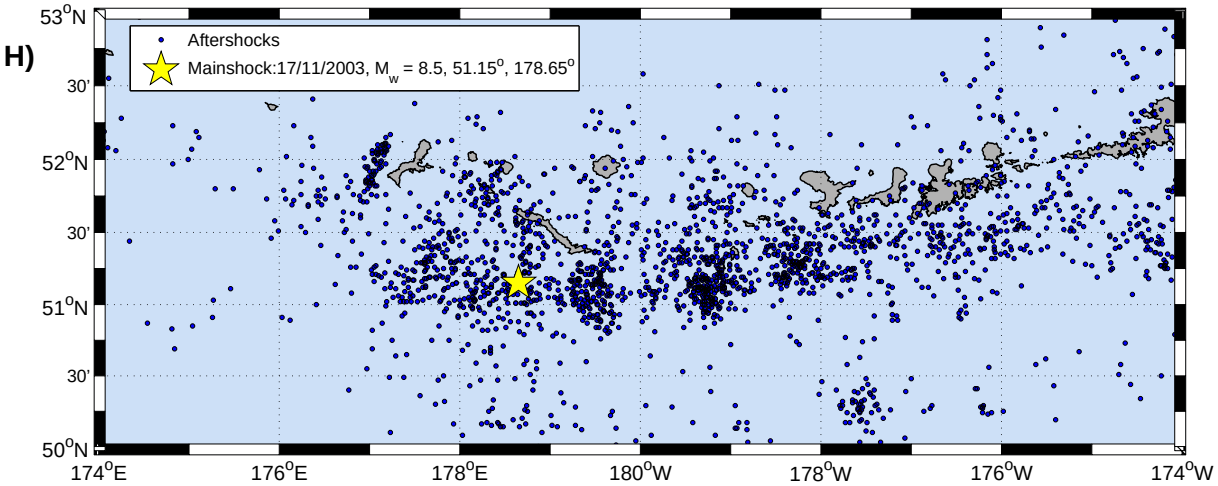

(h)

Figure 3.3: Maps showing spatial distribution of aftershocks chosen for G) Alaska 1, H) Alaska 2 datasets.

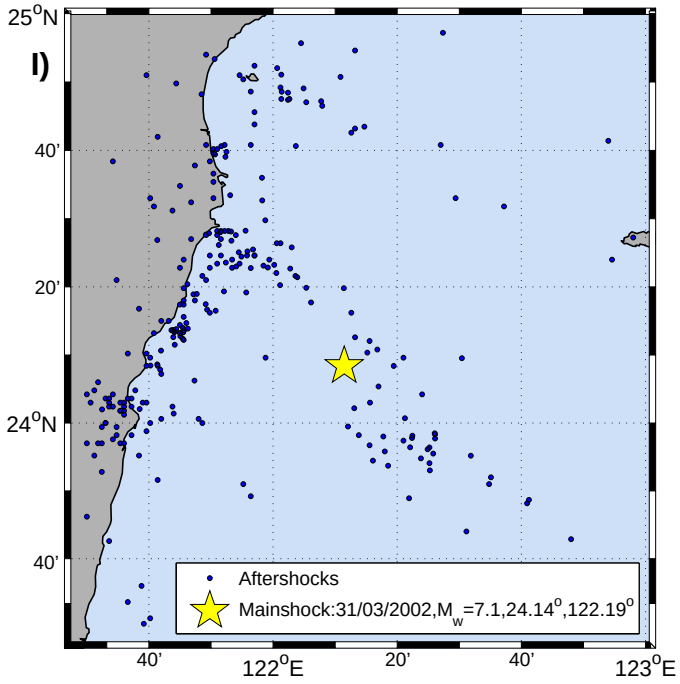

(i)

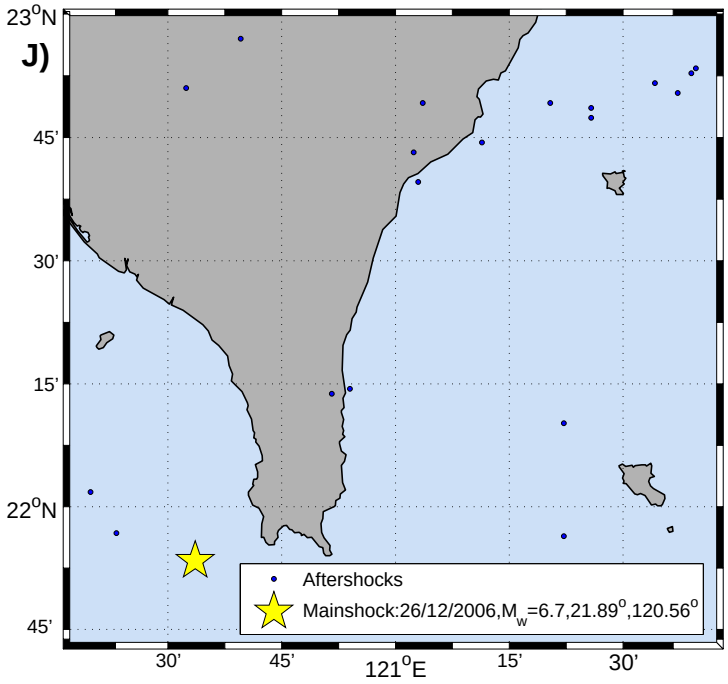

(j)

Figure 3.3: Maps showing spatial distribution of aftershocks chosen for I) Taiwan 1 and J) Taiwan 2 datasets.

Event Name (Event Tag)	M_c	b	S_1	S_2	RMS error	R square
Loma Prieta (L)	0.50	0.67	1.15	-	2.22	0.99
Kobe (K)	2.00	0.90	2.41	-	1.11	0.99
Sumatra (S)	3.63	0.81	4.16	-	5.18	0.99
Muzaffarabad (M)	3.33	0.79	4.05	-	7.38	0.99
Chamoli (C)	-0.20	0.32	1.39	-	2.02	0.99
Bam (B)	2.70	0.90	3.48	-	45.28	0.99
Zarand (Z)	2.80	0.99	3.47	-	10.11	0.99
Alaska 1 (Al 1)	3.00	1.08	-	3.47	12.78	0.99
Alaska 2 (Al 2)	2.60	0.46	-	3.47/4.08	9.41/11.37	0.99/0.99
Taiwan 1 (T 1)	3.42	0.77	4.30	-	39.55	0.99
Taiwan 2 (T 2)	3.63	0.75	4.32	-	17.73	0.99

Table 3.1. Event names are used to refer to respective sequences in the text. The event tags correspond to those in the plot in Figure 3.4 and Figure 3.5. S_1 corresponds to the slope of the linear fit with the homogeneous listings while S_2corresponds to the linear fit with the inhomogeneous datasets. In Alaska 2, the slope changes midway (see Figure 3.6(C)) and the two slopes, rms errors and R square values depict the values obtained while fitting for the earlier part before the slash and for the later part after the slash.

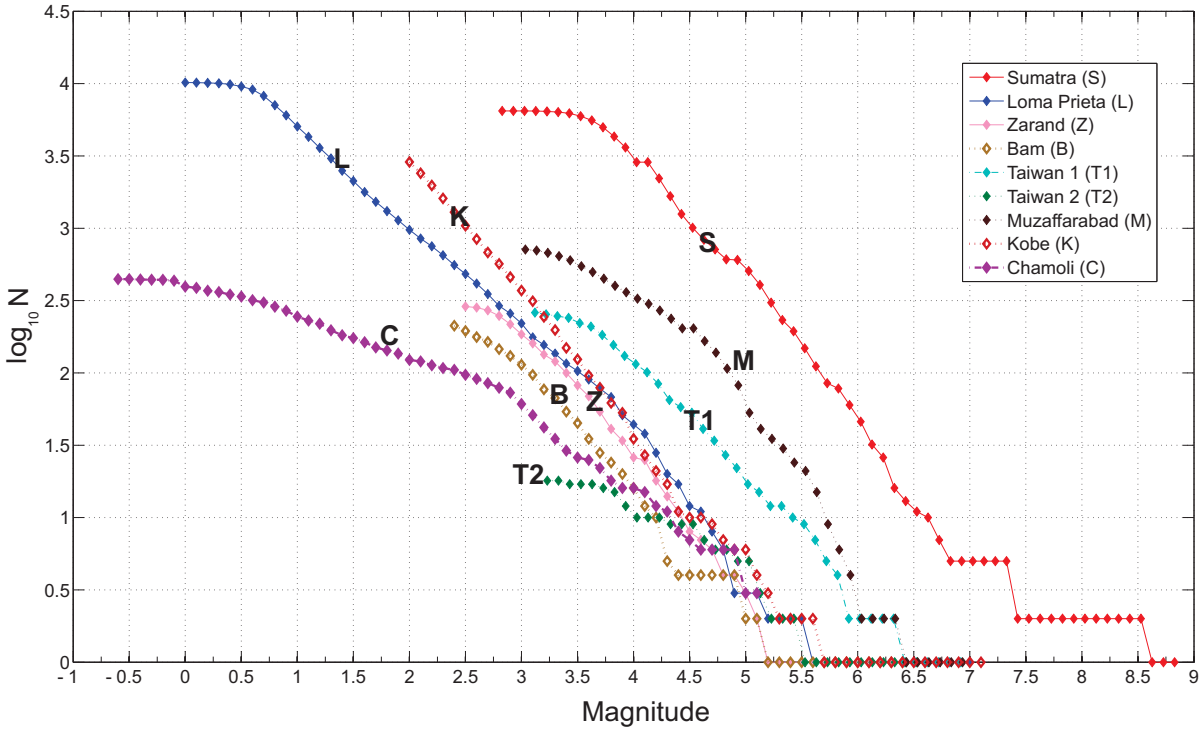

Figure 3.4: The Frequency-Magnitude distributions for the various aftershock sequences enlisted in Table 3.1 (except for the Alaska 1 and Alaska 2 sequences).

However, for the Alaska 2 listing no such clear maximal homogeneous subset was available and we calculated M_c and b based on the entire inhomogeneous dataset. This is followed by calculation of $Q(t)$ where the cumulative integral is carried out only over events that have magnitude $m \geq M_c$. Therefore in our case the minimum magnitude or lower cut off is M_c unless otherwise specified. Our analyses indicate a clear linear relationship $Q(t) = St$ where S denotes the slope. Wherever we have a homogeneous listing, we have attempted to fit a straight line to the observed $Q(t)$ curve and we call the slope thus obtained as S_1. Wherever we have a inhomogeneous listing the slope obtained by fitting is renamed as S_2. This is the nomenclature followed in Table 3.1 in listing the slopes for each sequence. The results of our analysis mentioned in Table 3.1 and the plots in Figure 3.1 point clearly to the linear variations mentioned above. The straight line (fit) retains this slope for years. Also the slope changes significantly over different fault zones. This indicates that the slope, S, is characteristic of the fault zone. This was further checked by integrating from anywhere in the time series (i.e. shifting our $t = 0$ to any randomly chosen aftershock) after the mainshock. The slope was found to be the same and the linearity of $Q(t)$ was not affected by shifting the origin of integration. A wide variety of events can lead to systematic errors in the reported magnitudes (events as varied as a change in instrumental calibration to addition or removal of seismograph stations) and such systematic errors can be very large going up to as much as 0.5 magnitude units [47]. Such errors would set the eventual error bound for the slope as the errors due to fitting are much smaller as stated already. Additionally, the conversion relationships themselves induce some errors in the magnitudes. This can also lead to systematic errors in the slope estimate. With the available catalogs, the errors in slope estimation would be thus about 6-10% [47, 48].

3.3.1. Analyzing the properties of the slope As we said earlier, it is our contention that these slopes are characteristic of the fault zone. Firstly, there is significant global variation in the values of the slopes. Each aftershock sequence seems to have a different slope for the $Q(t)$ statistic. Significantly, aftershock sequences caused by the same fault zone or on the same geologic and tectonic setting yield similar slopes. These two facts are clear from the results in Table 3.1. To illustrate the second point further, we draw attention to the two Taiwan sequences, Taiwan 1 and 2. Both of these took place on the Eurasian and Philippines plate boundary (from the Earthquake Summary Poster for the Taiwan event (26/12/2006, $M_W = 6.7$) available at (`http://earthquake.usgs.gov/eqcenter/eqarchives/poster/2006/20061226.php`). It is only natural that the two corresponding slopes would be nearly identical in view of our proposed error bounds due to the geological similarities and precisely similar tectonism. In Iran though, on the contrary, the Bam and Zarand earthquakes took place on two different faults belonging to a highly developed fault system. The Bam event occurred on the Bam fault whereas the Zarand event took place in close proximity of a previous event on the Gowk system (1981 July 28, Sirch earthquake $M_W = 7.1$) at a distance of about 60 km from the northern extremity of the rupture zone of the Sirch event [49]. But still the slopes were found to be the same (within proposed error bounds). This might be because the Gowk system and the Bam fault are part of a highly developed fault system. Further, the slope does not change with unusually large aftershocks in the sequence e.g. the Sumatra sequence had a few very large aftershocks including one great earthquake on March 28, 2005 ($M_W = 8.7$) which occurred about 150 km SE of the earlier giant earthquake epicenter ($M_W = 9.3$) of December 26, 2004. This further reveals the characteristic nature of the slope.

More importantly it is critical to note that the integration process is akin to an averaging process on the magnitudes and the slope, as we will later see, is approximately an average magnitude. So the reader may immediately think that the slope is more a signature of the catalog and the completeness level of the listing rather than the fault itself. But then if we have examples where reactivation or re-rupturing or similar events on a preexisting fault system

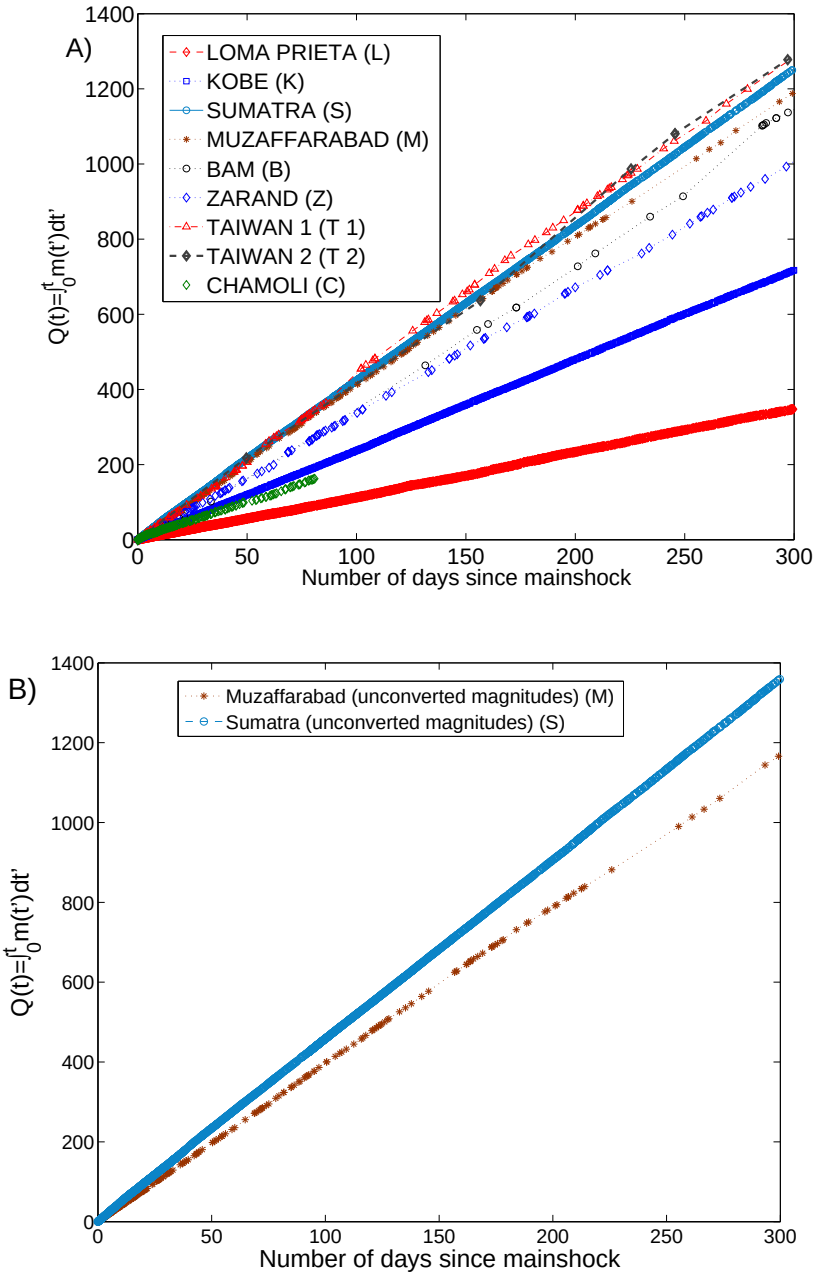

Figure 3.5: (A) Plots of time cumulant of magnitude $Q(t)$ vs. t (in number of days since the mainshock) for the datasets described in the text and in Table 1 for the first 300 days. The tags for the events used in the plot are the same as in Table 3.1. (B) Plots of $Q(t)$ vs. t for the Sumatra and Muzaffarabad sequences before conversion of magnitudes according to [31] and [46] respectively. Again, only the first 300 days are plotted.

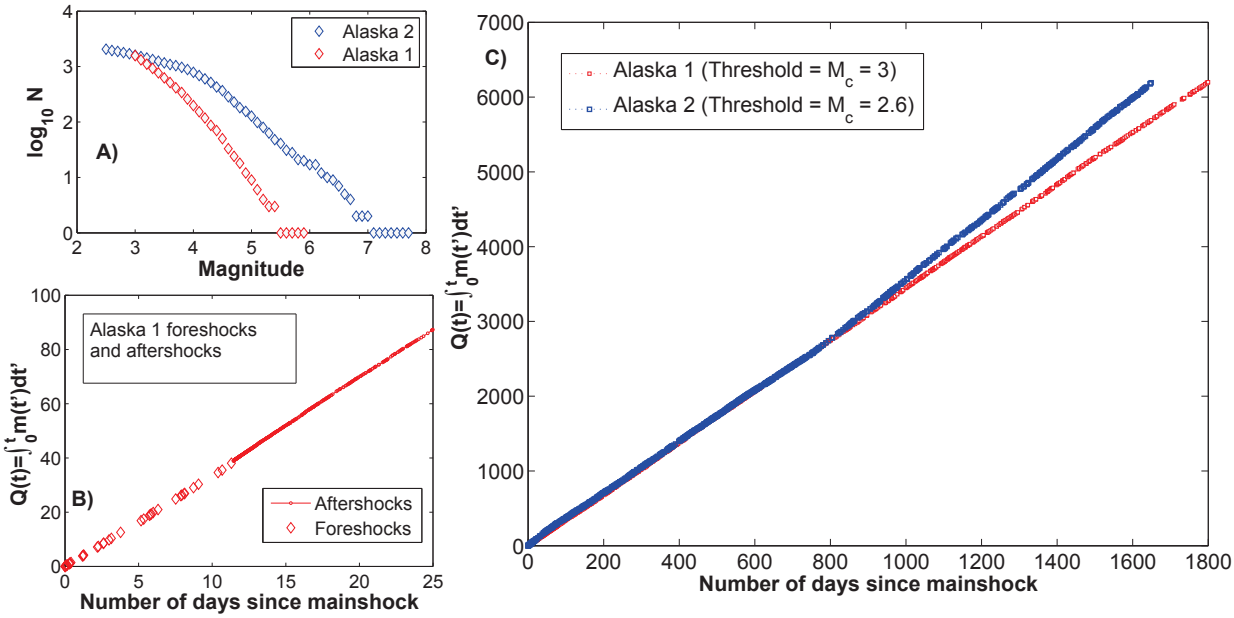

Figure 3.6: A) The frequency magnitude distribution (FMD) plots for Alaska 1 and Alaska 2. As noted in the text, the FMD for Alaska 1 is computed on the M_L listing. For Alaska 2 the FMD was calculated on the entire inhomogeneous listing. B) $Q(t)$ for the first 25 days for Alaska 1 showing that foreshocks and aftershocks exhibit same slope. C) The entire sequences for Alaska 1 and 2. Note slope change in Alaska 2.

changes the slope of $Q(t)$ over time, that would establish the characteristic nature of the slope. The reason for this is two fold. Firstly, as we will show later, we have considerable reason to believe that the slope of the $Q(t)$ statistic depends significantly on the geometry of the faults and the slope change is an expected result of the change in geometry of the fault surface due to the re-rupturing. Secondly, the inherent changes in completeness level in aftershock sequences are limited to within days of the occurrence of the mainshock. If we observe a change in slope a long time after the mainshock, when the M_c has stabilized to a steady level, then this change in slope cannot be ascribed to a change in completeness level. This slope change is then due to the changes in asperity distribution and stress patterns brought about by the re-rupturing. The reader will quickly recognize that this statement supports the analytical expression for the slope obtained in (2.16). Re-rupturing will clearly modify the slope as it would modify the nature of the fractal involved, either the dimension or q or the generation or n. If the slope changes due to these factors then of course it is characteristic of the fault involved. This part will become very clear later when we discuss the statistical interpretation of the slope as average magnitude. At present let us look at an example of such an occurrence which strengthens our claims. To this end we shall use the results for the two sequences obtained in Alaska. Alaska 1 was an event on the inland Denali fault and the $Q(t)$ statistic gives a slope $S_2 = 3.47$. One important aspect came out during the analysis of the Alaska 1 dataset. The first shock considered here was not the Denali fault mainshock but a previous shock in the same region. This was done because this event is a very well established foreshock of the Denali fault event and is followed by a series of foreshocks till the occurrence of the mainshock. The cumulant $Q(t)$ for the foreshocks retains the same linearity as the cumulant $Q(t)$ for the aftershocks (see Figure 3.6 (B)). This is expected though if one believes in the characteristic nature of the slope for a given fault system.

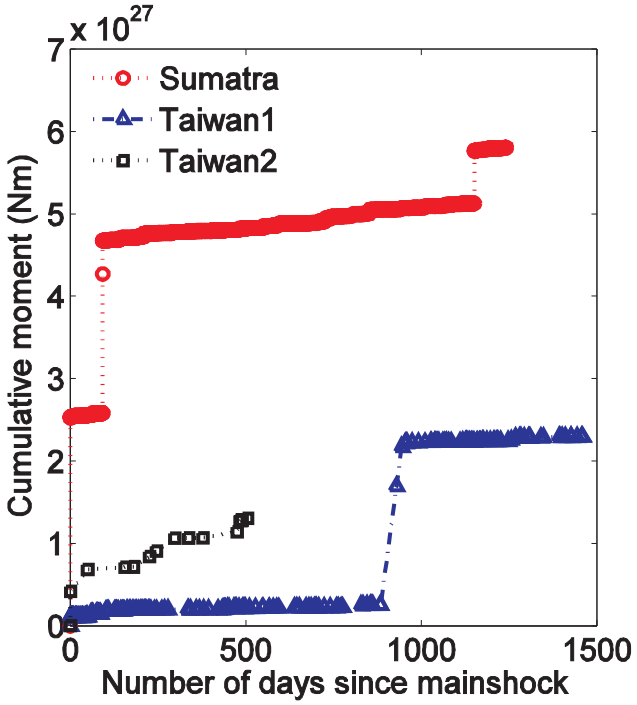

Figure 3.7: Plots of cumulative moment versus time since the mainshock for the datasets Sumatra, Taiwan 1 and Taiwan 2. The values for Taiwan 2 depicted here in the plot are 10 times the real values to ensure proper legibility of the figure (cf. [17]).

As foreshocks and aftershocks both happen on the same fault or fault system they are expected to yield the same slopes. Our claim, that the slope is a signature of the fault system, is further strengthened on analysis of the Alaska 2 aftershock sequence (see Figure 3.6 (C)). Here, the slope of the $Q(t)$ vs. t curve increases after about 754 days of the main event. One of the most significant events of the last century, the 1965 M_w 8.7 Rat Islands earthquake ruptured a 600 km long portion of the plate boundary to the west of the Amchitka Island. In the November 17, 2003 M7.7 earthquake, associated with the main shock or the first shock in the sequence we chose, the easternmost part of the 1965 zone failed again. On June 14, 2005, a series of moderate to strong earthquakes occurred in the Rat Islands region of the Aleutian Islands. The sequence started with a M 5.2 event at 08:03 UTC and the largest event (M 6.8) followed 9 hours later (at 17:10 UTC). The largest earthquake was situated 49 kilometers (31 miles) south-southeast of Amchitka. This new sequence of earthquakes re-ruptured the easternmost end of the 1965 rupture zone. This is the reason, we believe, for the increase in slope. The re-rupturing process meant that the earlier asperity distributions were changed and hence the region underwent a marked change in its seismicity pattern. The slope measures for the Alaska 2 sequence are given in Table 3.1 for the total inhomogeneous event listing i.e. $S_2 = 3.47$ for the earlier half and $S_2 = 4.08$ for the later half. The change in slope, as one can clearly observe is not within our error bounds. The slope change also occurs after about two years from the mainshock and hence should not be an artifact of change in minimum completeness level of the seismic network which is constant by now. Also the slope does not keep on changing and remains at $S_2 = 4.08$ for the rest of the sequence. The slope of $Q(t)$ definitely shows that some significant change occurred in the aftershock sequence (equivalently the fault system) due to re-rupturing.

However such cumulative statistics have already been attempted for the scalar seismic moment or Benioff stresses for aftershock sequences. We did a similar cumulative integral of scalar seismic moment for our sequences in Sumatra and Taiwan (the former was reliably converted to scalar

seismic moment in [31] and the BATS CMT catalog for Taiwan was homogeneous and listed only broadband M_W values). The results are shown in the Figure 3.7. The resultant plots resemble a step function. Authors in [31] have tried to fit a power law and/or linear models piecewise to such data (in their case the cumulative Benioff stress). There seems to be no robust feature to this statistic, i.e. the cumulative moment versus time curve. Such cumulative curves have also been reported for theoretical models such as for the Critical Continuum-State Branching Model of Earthquake Rupture [50]. Precursory accelerating moment release before large earthquakes has been a widely discussed phenomenon until recent years, being regarded as observational evidence for the controversial critical-point-like model of earthquake generation [51, 52]. Another useful property of such seismic moment cumulants is that they help in monitoring the stress release modes for a given region and hence allow for discussions on the type of mechanisms underlying earthquake occurrences [53].

As mentioned earlier, the slope of $Q(t)$ is an estimate of the average magnitude of the aftershock sequence. We proceed on this line and try to obtain an expression connecting the slope and other parameters of aftershock statistics. For an aftershock sequence, apart from the first few aftershocks, let us assume that the event inter-occurrence times and their magnitudes are statistically independent of each other in the long term. Then for a large number of events we have,

$$Q(t) = \int_0^t m(t')dt' \approx \int_0^t \overline{m}(t')dt' \approx \overline{m}t, \tag{3.2}$$

where $\overline{m}$ is the average magnitude calculated from the GR distribution for the aftershock sequence (assuming that the b value is constant over time which is an observed fact [22]). Now this $\overline{m}$ can be calculated from the GR distribution as follows,

$$\overline{m} = \int_{m_{\min}}^{m_{\max}} m \frac{b \times \ln 10 \times 10^{-bm}}{(10^{-bm_{\min}} - 10^{-bm_{\max}})} dm. \tag{3.3}$$

If we assume that the GR law holds for all larger magnitudes then $m_{\max}$ tends to infinity and we have,

$$S = \overline{m} = m_{\min} + \frac{0.43}{b}. \tag{3.4}$$

This is the expression for the slope which connects it with the b value for the aftershock sequence. We have presented a comparison of the slopes obtained through fitting and $\overline{m}$ in Table 3.2 (except for the Alaska 2 sequence because of the complete inhomogeneity and change in slope midway). The results show a very good agreement. But the agreement is in general better for b as computed for the specific aftershock sequence rather than the global b value of unity. In some cases like in Loma Prieta, Taiwan 2 and Chamoli the error (i.e. $S - \overline{m}$) for $b \neq 1$ is an order of magnitude less than the errors obtained when $\overline{m}$ is computed using $b = 1$. Clearly, in general $S = \overline{m}(b)$ is a more accurate expression than $S = \overline{m}(b = 1)$. This brings us to an important realization. As can be seen in Table 3.1 and is also reported widely [22], the b-values for individual aftershock sequences are unique to the sequence in general and show wide variations. Moreover the b-value for a single aftershock sequence has been known to vary spatially between the extremities of the rupture [22].

However, temporally, the b-value is exceptionally robust except at times when we have rather large earthquakes. Now it is known that the b-value of a given aftershock sequence can be explained in terms of the surface similarity dimension of the causative fault network (the fault network being treated as a fractal) [54]. Also the Two Fractal Overlap model clearly demonstrates the GR law for the synthetic aftershock sequences and shows that the b-value

Event Tag	M_c	b	$\overline{m}(b=1)$	$\overline{m}(b)$	S	$S-\overline{m}(b=1)$	$S-\overline{m}(b)$
L	0.50	0.67	0.93	1.14	1.15	0.22	0.01
K	2.00	0.90	2.43	2.47	2.41	-0.02	-0.06
S	3.63	0.81	4.08	4.18	4.16	0.08	-0.02
M	3.33	0.79	3.78	3.90	4.05	0.27	0.15
C	-0.20	0.32	0.33	1.23	1.39	1.06	0.16
B	2.70	0.90	3.13	3.18	3.48	0.35	0.30
Z	2.80	0.99	3.23	3.24	3.47	0.24	0.23
Al 1	3.00	1.08	3.43	3.40	3.47	0.04	0.07
T 1	3.42	0.77	3.95	4.03	4.30	0.35	0.27
T 2	3.63	0.75	4.16	4.30	4.32	0.16	0.02

Table 3.2. The comparison of S and $\overline{m}$ computed from (3.4) using $b = 1$ (values listed as $\overline{m}(b = 1)$) as well as using b as computed by us from the sequences (values listed as $\overline{m}(b)$). $m_{\min} = M_c$ for all the sequences. The errors are listed as $S - \overline{m}$.

is purely dependent on the dimension and generation of the fractals involved in sticking and slipping (in our case we have the dependence on the fractal dimension). In the case of real aftershock sequences this would be equivalent to saying that the b-value is dependent on the fractal geometry of (a) the fault surfaces (b) the fault network. Therefore, the b-value might change after a large earthquake due to re-rupturing or extensive change in asperity distributions. Re-rupturing would affect the fractal geometry of the fault and, as discussed before, this should generally increase the slope of the $Q(t)$ statistic (not decrease). This is what we believe happened in Alaska 2. So as S is a function of the b-value it is characteristic of the fault geometry. Also one must keep in mind that our definition of the completeness magnitude is dependent on the roll-off of the frequency-magnitude distribution from the GR law curve towards the lower magnitude range. Our definition of a roll off or a fitting algorithm (like the one we used), based on creating synthetic distributions with the b-value obtained, depend on the value of b and a slightly smaller or larger b can alter our M_c calculations and hence affect our chosen $m_{\min}$. Theoretically, we also saw that the roll off can be defined as a log correction on the GR law and its onset is defined by the factor $n/3$, the same factor which decides the slope. Hence the roll off itself is a function of the generation number for the Cantor set or the geometry and extent of rupture of the fault. Thus the slope can be clearly called a definite characteristic of the fault zone as it is highly affected by the b-value. The usual temporal stability of the b-value explains the constancy in slope over long periods of time. The other question that we tried to address is: Is equation (3.4) an accurate expression for S or a good approximation? To check this we used the following observation. If we increase our $m_{\min}$ by some $\Delta m_{\min}$ above the minimum level of completeness then, we have, using (3.4),

$$\Delta S = \Delta\overline{m} = \Delta m_{\min} + \Delta\left(\frac{0.43}{b}\right). \tag{3.5}$$

Now as b is constant above the completeness level the second term on the right hand side goes to zero and we have,

$$\Delta S = \Delta m_{\min}. \tag{3.6}$$

We checked for this by recalculating $Q(t)$ for three different minimum magnitude thresholds for each sequence. We chose $m_{\min} = M_c + \Delta, \Delta = 0, 0.1$ and 0.2 as thresholds for each sequence. Nowhere did the results agree exactly to (3.6). Close agreement was seen only for Alaska 1. The results are reported in Table 3.3 and the plots for Muzzafarabad and Loma Prieta are shown in Figure 3.8. This implies that (3.4) might be an over-simplified expression for the slope and is not

Event Tag	M_c	$S(m_{\min} = M_c)$	$S(m_{\min} = M_c + 0.1)$	$S(m_{\min} = M_c + 0.2)$
L	0.50	1.15	1.17	1.21
K	2.00	2.41	2.49	2.57
S	3.63	4.16	4.21	4.28
M	3.33	4.05	4.08	4.10
C	-0.20	1.39	1.40	1.47
B	2.70	3.48	3.53	3.59
Z	2.80	3.47	3.48	3.55
Al 1	3.00	3.47	3.56	3.63
T 1	3.42	4.30	4.31	4.38
T 2	3.63	4.32	4.42	4.43

Table 3.3. Effect of the increment in $m_{\min}$ on the fitted slope of Q(t) for all the sequences in Table 3.2.

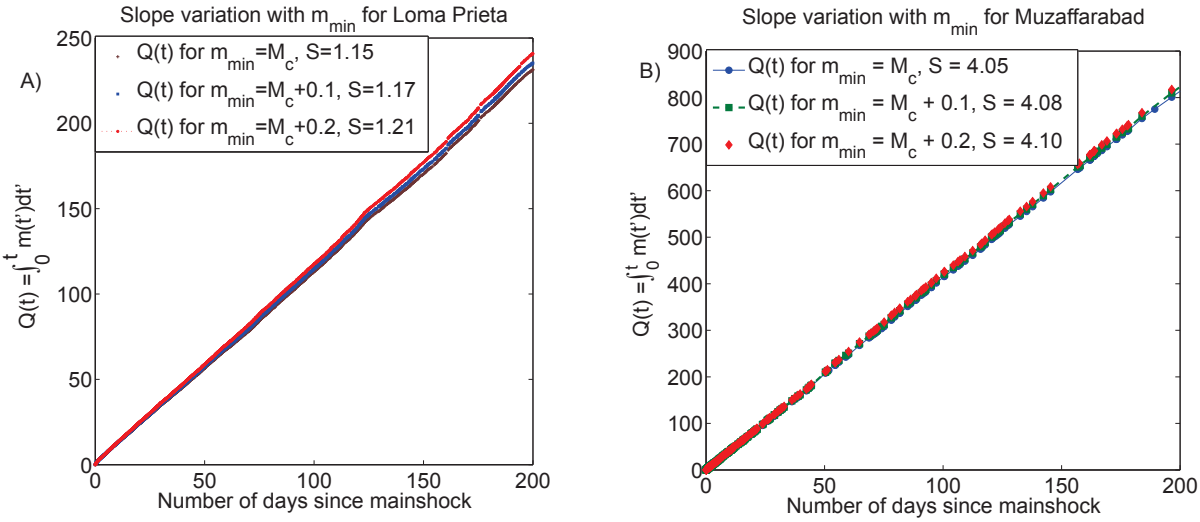

Figure 3.8: Slope variation in $Q(t)$ with $m_{\min}$ for the aftershock sequences in Loma Prieta and Muzaffarabad. First 200 days shown for the sake of clarity.

accurate. It explains the dependence of the slope on b reasonably whereas the dependence of the slope on $m_{\min}$ seems not to be straightforwardly linear. Hence the slope is probably not simply a manifestation of the lower magnitude cut-off. The failure of (3.4) and (3.6) to address the slope increment may also be an indication that aftershock magnitudes and inter-occurrence times may not be uncorrelated even long after the mainshock thus invalidating the line of mathematical argument used to arrive at (3.4).

3.3.2. Possible usefulness of the slope To end our discussion we check the nature of the linearity of the $Q(t)$ statistic: Is it deterministic or stochastic? We check this using the following expression for the numerical evaluation of the integral for $Q(t)$;

$$Q(t_i) = \int_0^{t_i} m(t')dt' \approx \sum_i m(t_i)\Delta t_i = Q(t_{i-1}) + m(t_i)(t_i - t_{i-1}) \tag{3.7}$$

which leads to the expression

$$t_{i+1} = \frac{m(t_{i+1})t_i - Q(t_i)}{m(t_{i+1}) - S}, \tag{3.8}$$

where we make use of the fact that $Q(t_{i+1}) = St_{i+1}$. For all the aftershock sequences, as a benefit of posteriori knowledge of the catalog sequence, we have with us $m(t_{i+1})$ as well as t_{i+1}. So starting with the mainshock and using the magnitudes of every subsequent aftershock we could make a synthetic occurrence time listing of t_{i+1} using (3.8) for each i. This synthetic t_{i+1} we will call $t_{\rm pred}$ while the actual catalog listed sequence of t_{i+1} we call $t_{\rm ac}$. We calculated the quantity $t_{\rm pred} - t_{\rm ac}$ and created scatter plots against $t_{\rm ac}$. The plots had very significant concentration of points around the line $y = t_{\rm pred} - t_{\rm ac} = 0$ but there were also some very large outliers. In general though the number of deviations were quite smaller. The concentration of most of the points around $t_{\rm pred} - t_{\rm ac} = 0$ clearly demonstrates the deterministic nature of the linearity. The details of the behavior of such plots will be discussed by us elsewhere. At the present we give two such plots for the Kobe and Muzaffarabad sequences to demonstrate this point. As pointed out earlier, the linearity in $Q(t)$ is maintained with the same slope if we shift our origin of integration to any aftershock in the sequence. As cumulative integrals are always subject to accumulation of errors, we also recalculated $t_{\rm pred}$ within various time windows within the series where the origin of the window is far from the mainshock. We observed lesser scatter within the time window than that observed within the same time window when the origin of integration was the mainshock indicating lesser error accumulation as expected. One usefulness of this result is that if we have apriori knowledge of (or we assume) the magnitude of the next aftershock in a sequence then (3.8) can be used in real time to predict time of occurrence by extrapolation (which makes perfect sense for this linear curve). Conversely we can have prediction tables where we can obtain a list of occurrence times for the next aftershock corresponding to a list of possible magnitudes of the event. We will discuss the prediction issue in more detail elsewhere. In real time calculations we can minimize errors by shifting our origin of integration or in other words putting $Q(t) = 0$ after every few aftershocks and recalculating all parameters in (3.8) again by again allowing $Q(t)$ to accumulate over the next few aftershocks and so on. This aspect of our study shows that the linearity of the $Q(t)$ statistic is deterministic and not stochastic. This affords it the unique ability to predict occurrence times of aftershocks given an estimate of the magnitude of the next event (which, as far as we know, is not possible by our current state of knowledge).

4. Conclusion

We have presented here some new results that have come out from our analysis of the Two Fractal Overlap model. The model is based on the fact that fault surfaces, both fresh and weathered, exhibit a fractal topography (Section 1.2). The model captures the stick-slip dynamics of overlapping fractal surfaces by using regular middle third removal Cantor sets (Section 2.1) wherein a Cantor set of a given generation slides over its replica with uniform velocity. Our model is essentially one of repeating seismicity on the same fault following a large magnitude event (or aftershocks). The statistical features of the synthetic earthquake time series thus produced are completely analytically tractable (Section 2.2). The model, as is evident from our

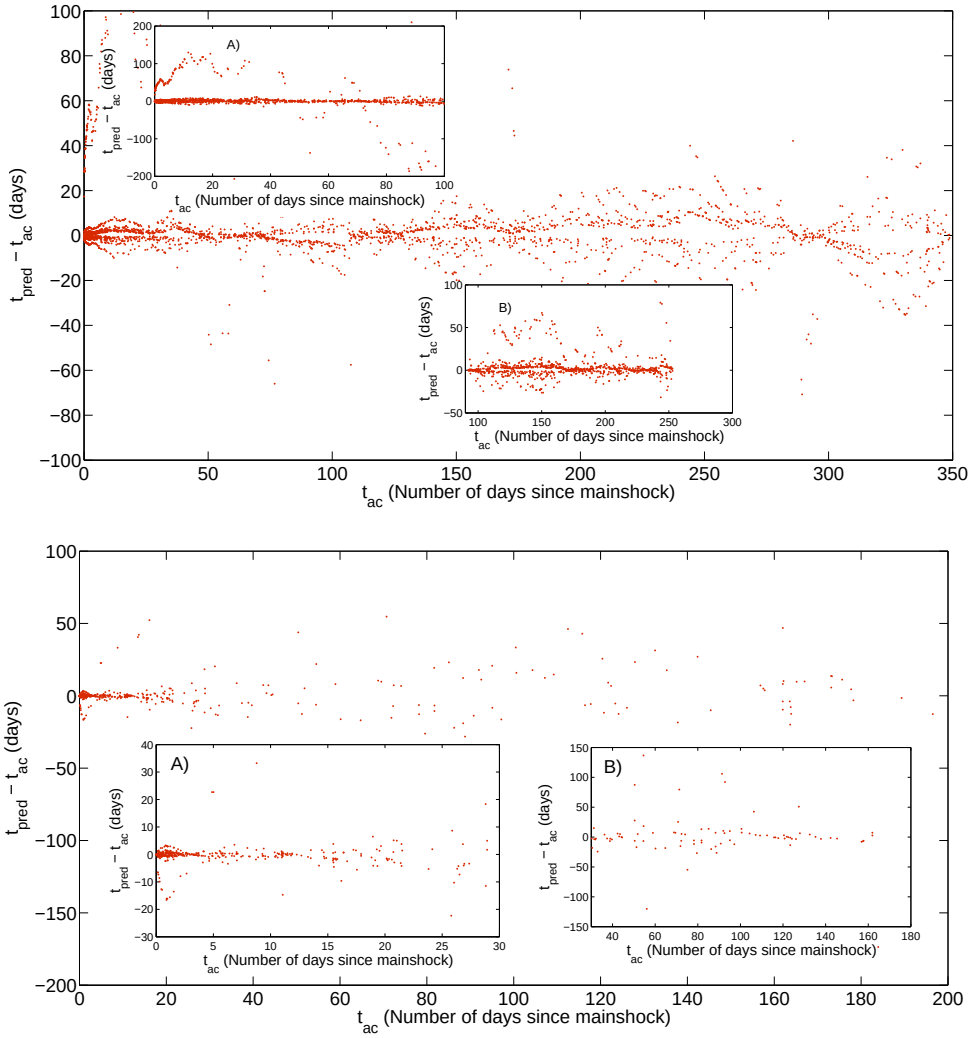

Figure 4.9: The $t_{\rm pred} - t_{\rm ac}$ vs. $t_{\rm ac}$ plots for the Kobe (top) and Muzaffarabad (bottom) sequences for first 350 and 200 days respectively. Some of the larger deviations from $y = t_{\rm pred} - t_{\rm ac} = 0$ lie beyond the extent of the y-axis shown here and are omitted to facilitate better viewing. Inset: different time windows within which $Q(t)$ was recalculated. For Kobe: Inset A) First 100 days only. Inset B) Between 90 and 250 days. Scatter lessened significantly with respect to the same time window when we integrate $Q(t)$ from the aftershock at the time origin of the window rather than the mainshock. For Muzaffarabad: Inset A) First 30 days. Inset B) Between 30 to 160 days. Again note the reduced scatter with respect to the same time window when we integrate $Q(t)$ from the aftershock at the time origin of the window rather than the mainshock.

analysis, captures the GR law (Section 2.3). If one agrees that aftershock time decay is given by the Omori law and not the modified Omori Law, then the model also captures the rudimentary features of this behavior (Section 2.4). It gives a hitherto unknown statistical feature of the temporal distribution of aftershock magnitudes which we have shown in Section 2.5. The model predicts that the time cumulant of magnitudes of synthetic seismicity produced by the model for a given generation number is a remarkable straight line with a slope that is characteristic of the fractal topography of the rupture surface. In Section 3 we have shown the proximal correspondence of the values of the model parameters with the b-value and the constant a in the GR law as observed for natural seismicity. The model also shows that there may be some

physical basis behind the completeness magnitude M_c and the corresponding low magnitude roll off of the frequency magnitude statistics of earthquakes. There is also reasonable analogy between the behavior of the exponent p in Omori Law and the exponent which describes time decay of aftershocks in this model.

We have also shown that the new statistical law involving the time cumulant of magnitudes discussed in Section 2.5 is also observed in nature in the case of aftershocks and this might give us important information about the fractal geometry of the faults involved in producing an earthquake and its aftershock sequence. Specifically, we have shown that cumulative integral of magnitudes $Q(t)$ of a natural aftershock sequence over time t is linear, the slope S being characteristic of the fault zone. Hence some key features of the rupture zone may be extracted from such an analysis of the magnitude time series $m(t)$ of the earthquake aftershocks, in particular information about the fractal geometry of the fault. We have demonstrated the characteristic property of the slope and its relationship with the b value. We have also shown that though the slope depends on the lower magnitude cutoff, the relationship is not very simple or linear. More importantly we have demonstrated that the linearity of $Q(t)$ is deterministic and hence might very well provide methods to predict aftershock occurrence times in the future

Our focus here was on the Two Fractal Overlap Model which is a very simplistic model of earthquakes and do not claim in any way that this is the realistic physical scenario at the geological faults. But the fact that such a simplistic geometrical model mimics so much of nature is truly astonishing. The analysis, we reiterate, is one which requires very basic mathematics. The fractal overlap model tells us that the role of the fractal geometry of fault surfaces might play a significant role in controlling the statistical features of aftershock sequences.

References

[1] Gutenberg B and Richter C F 1944 *Bull. Seismol. Soc. Am.* **34** 185–188
[2] Omori F 1894 *J. Coll. Imp. Univ. Tokyo* **7** 111
[3] Utsu T, Ogata Y and Matsuura R S 1995 *J. Phys. Earth* **43** 1–33
[4] Burridge R and Knopoff L 1967 *Bull. Seismol. Soc. Amer.* **57** 341–371
[5] Carlson J M, Langer J S and Shaw B E 1994 *Rev. Mod. Phys.* **66** 657–670
[6] Olami Z, Feder H J S and Christensen K 1992 *Phys. Rev. Lett.* **68** 1244
[7] Bak P, Tang P and Weisenfeld K 1987 *Phys. Rev. Lett.* **59** 381
[8] De Rubeis V, Hallgass R, Loreto V, Paladin G, Pietronero L and Tosi P 1996 *Phys. Rev. Lett.* **76** 2599
[9] Hallgass R, Loreto V, Mazzella O, Paladin G and Pietronero L 1997 *Phys. Rev.* E **56** 1346
[10] Aochi H and Matsuura M 2002 *Pure Appl. Geophys.* **159** 2029–2044
[11] Sagy A, Brodsky E E and Axen G J 2007 *Geology* **35** 283
[12] Power W E, Tullis T E, Brown S R, Boitnott G N and Scholz C H 1987 *Geophys. Res. Lett.* **14** 29
[13] Brown S R and Scholtz S H 1985 *J. Geophys. Res.* **90** 12575
[14] Chakrabarti B K and Stinchcombe R B 1999 *Physica* A **270** 27
[15] Bhattacharyya P 2006 Geometrical models of earthquakes *Modeling Catastrophic and Critical Phenomena in Geoscience: A Statistical Physics Approach* ed Bhattacharyya P and Chakrabarti B K (Springer-Verlag) pp 155–168
[16] Pradhan S, Chakrabarti B K, Ray P and Dey M K 2003 *Phys. Scripta* **T106** 77
[17] Bhattacharya P, Chakrabarti B K, Kamal and Samanta D 2010 Fractal models of earthquake dynamics *Reviews of Nonlinear Dynamics and Complexity* vol 2 ed Schuster H G (Wiley-VCH Verlag GmbH & Co. KGaA) chap 4, pp 107–158 ISBN 9783527628001 URL `http://dx.doi.org/10.1002/9783527628001.ch4`
[18] Abramowitz M and Stegun I 1964 *Handbook of Mathematical Functions* 5th ed (New York: Dover)
[19] Okubo P G and Aki K 1987 *J. Geophys. Res.* **92** 345–356
[20] Scholz C H 1990 *The Mechanics of Earthquakes and Faulting* (Cambridge University Press, New York)
[21] Wiemer S and Wyss M 1997 *J. Geophys. Res.* **102** 15115–15128
[22] Wiemer S and Wyss M 2002 *Adv. Geophys.* **45** 259
[23] Schorlemmer D, Wiemer S and Wyss M 2005 *Nature* **437** 539–542
[24] Utsu T 1969 *J. Fac. Sci. Hokkaido Univ.* **3** 129
[25] Bhattacharya P, Phan M and Shcherbakov R 2011 *Bull. Seismol. Soc. Am.* In Press
[26] Hirata T 1986 *Zishin (J. Seismol. Soc. Japan)* **39** 478 in Japanese
[27] Kisslinger C and Jones L M 1991 *J. Geophys. Res.* **96** 11947–11958
[28] Wiemer S and Wyss M 2000 *Bull. Seismol. Soc. Am.* **90** 859–869
[29] Peng Z G, Vidale J E and Houston H 2006 *Geophys. Res. Lett.* **33** L17307
[30] Kanamori H 1977 *J. Geophys. Res.* **82** 2981
[31] Jiang C and Wu Z 2006 Pre-shock seismic moment release in different segments of a fault: the case of the 26 December 2004 Indonesia Mw = 9.0 earthquakes *Advances in Geosciences* vol 1 (Solid Earth) ed Ip W H (World Scientific, Singapore)

[32] Kamal and Mansinha L 1996 *Bull. Seismol. Soc. Am.* **86** 299

[33] Kamal and Chabak S K 2002 *J. Him. Geol.* **23** 63

[34] Mogi K 1962 *Bull. Earthquake Res. Inst.* **40** 125–173

[35] Das S and Scholz C H 1981 *J. Geophys. Res.* **86** 6039–6051

[36] Mikumo T and Miyatake T 1979 *Geophys. J. R. Astron. Soc.* **59** 497–522

[37] Scholz C H 1968 *Bull. Seismol. Soc. Am.* **58** 1117–1130

[38] Narteau C, Shebalin P and Holschneider M 2002 *J. Geophys. Res.* **107** 2359

[39] Nur A and Booker J R 1971 *Science* **175** 885–887

[40] Schaff D P, Beroza G C and Shaw B E 1998 *Geophys. Res. Lett.* **25** 4549–4552

[41] Dieterich J 1994 *J. Geophys. Res.* **99** 2601–2618

[42] Kagan Y Y 2004 *Bull. Seismol. Soc. Am.* **94** 1207–1228

[43] Perfettini H and Avouac J P 2004 *J. Geophys. Res.* -Solid Earth **109** B06402

[44] Shcherbakov R, Turcotte D L and Rundle J B 2004 *Geophys. Res. Lett.* **31** L11613

[45] Toda S, Stein R S, Reasenberg P A, Dieterich J H and Yoshida A 1998 *J. Geophys. Res.* **103** 24543

[46] PMD and Norsar 2007 Seismic hazard analysis and zonation for Pakistan, Azad Jammu and Kashmir Tech. rep. Pakistan Meteorological Department and Norsar, Norway

[47] Castellaro S, Mulargia F and Kagan Y Y 2006 *Geophys. J. Int.* **165** 913

[48] Sipkin S A, Person W J and Presgrave B W 2000 Earthquake bulletins and catalogs at the USGS National Earthquake Information Center Tech. rep. U.S.Geological Survey National Earthquake Information Center URL `www.neic.usgs.gov`

[49] Nalbant S S, Steacy S and McCloskey J 2006 *Geophy. J. Int.* **167** 309

[50] Kagan Y Y 2006 Why does theoretical physics fail to explain and predict earthquake occurrence? *Modeling Catastrophic and Critical Phenomena in Geoscience: A Statistical Physics Approach* ed Bhattacharyya P and Chakrabarti B K (Springer-Verlag)

[51] Sornette D and Sammis C G 1995 *J. Phys.* I **5** 607

[52] Jaume S C and Sykes L R 1999 *Pure Appl. Geophys.* **155** 279

[53] Fukuyama E, Kubo A, Kawai H and Nonomura K 2001 *Earth Planets Space* **53** 1021

[54] Turcotte D L 1997 *Fractals and Chaos in Geology and Geophysics* (Cambridge Univ. Press, Cambridge)